Rheology of suspensions of cubic particles

E d'Ambrosio, D Gilbert, F Blanc, C Cohen, Elisabeth Lemaire

Rheology of suspensions of cubic particles

E. d'Ambrosio, D. Gilbert, F. Blanc, C. Cohen, and E. Lemaire[1, a)]

Institut de Physique de Nice, UMR 7010, CNRS, Université Côte d'Azur, 17, rue Julien Lauprêtre, 06200 Nice, France

(Dated: 13 August 2025)

The rheology of non-Brownian suspensions containing non-spherical particles, such as cubes, remains largely unexplored, despite their relevance in both industrial and natural contexts. While many studies have focused on suspensions of spherical particles, only a few have investigated the viscosity of suspensions with cubic-like particles, and none have quantified the particle normal stresses in such systems. In this work, cubic particles were fabricated using a soft lithography technique and suspended in a Newtonian fluid. Rheometric experiments were conducted to determine the Einstein and Batchelor coefficients in the dilute and semi-dilute regimes, revealing stronger hydrodynamic interactions compared to spheres. In the concentrated regime, viscosity measurements as a function of shear stress exhibit shear-thinning behavior, which can be effectively captured by introducing a shear-dependent jamming volume fraction. The viscosity is significantly higher —or equivalently, the jamming fraction markedly lower— than in spherical particle suspensions. The third normal stress component (in the vorticity direction) is measured through resuspension experiments. We show that, for a given shear stress, the sediment spreads significantly more in suspensions of cubes than in suspensions of spheres, indicating substantially higher particle normal stresses than in the spherical case. Finally, at a given solid fraction, the ratio of the third particle normal stress to the shear stress is found to be of the same order for suspensions of spherical and cubic particles.

[a)]Corresponding author: elisabeth.lemaire@univ-cotedazur.fr

I. INTRODUCTION

Non-Brownian suspensions made of rigid particles are ubiquitous in industry (cosmetics, civil engineering etc...) and in natural flows (mud, submarine avalanches, lava flows etc.). This widespread occurrence has encouraged active research in the past years that has revealed great complexity in the behavior of these systems. Most studies deal with suspensions of spherical particles while, in many applications (fresh concrete, solid rocket fuel, chocolate etc.), particles have faceted shapes, making them more cube-like than spherical. Understanding the rheology of suspensions of non-spherical particles is then crucial. However, very few works have examined the viscosity of suspensions of non-spherical particles, and, to our knowledge, no prior study has measured particle normal stresses in such suspensions of cubic-like particles.

One of the most well-known features of suspension rheology is the increase in relative shear viscosity, $\eta_s = \Sigma_{12}/(\eta_0\dot{\gamma})$, , with increasing solid volume fraction, ϕ. Here, $\dot{\gamma}$ denotes the shear rate, and the indices 1, 2, and 3 refer to the flow, velocity gradient, and vorticity directions, respectively.

In the case of extremely dilute suspensions ($\phi \lesssim 0.01$), where particle interactions are negligible and hydrodynamic interactions between pairs can be ignored, Einstein [1] established the following equation for suspensions of spherical particles:

$$\eta_s = 1 + [\eta]\phi \text{ with } [\eta] = \frac{5}{2} \tag{1}$$

The coefficient $[\eta]$, which will be also denoted K_E in the present paper, is known as the "intrinsic" viscosity of the suspension and defined as: $[\eta] = \lim_{\phi \to 0}(\eta_s - 1)$. More than half a century later, Batchelor expanded Einstein's relation by accounting for hydrodynamic pairwise interactions and showed that, for $\phi \lesssim 0.1$, the viscosity follows[2]:

$$\eta_s = 1 + K_E\phi + K_B\phi^2 \tag{2}$$

Batchelor determined $K_B = 7.6$ for a suspension of spheres with weak Brownian motion in a pure shear flow (while $K_E = [\eta] = 2.5$)[2].

As ϕ increases and exeeds a typical value of 0.1, empirical relations are generally used to describe the variation of η_s with ϕ. The viscosity is known to diverge as the volume fraction approaches a maximum value, referred to as the jamming volume fraction, denoted ϕ_m. One of the most widely used laws in the literature was proposed by Maron and Pierce [3] and is defined as

follows:

$$\eta_s(\phi) = (1 - \phi/\phi_m)^{-2} \tag{3}$$

The exact value of ϕ_m varies from one system to another and depends on the contact properties of the particles. The presence of adhesive forces between particles[4–6] tends to increase the viscosity at a given particle volume fraction and consequently decreases the jamming fraction. Solid friction between particles also decreases the value of the jamming volume fraction as demonstrated by the pioneering works of Mari *et al.*[7], Seto *et al.*[8] on the discontinuous shear-thickening, and those of Gallier *et al.*[9] on the effect of friction on the rheology of non-Brownian suspensions.

Most non-Brownian suspensions exhibit rate-dependent rheology. The most well-known and arguably the most striking example is shear-thickening[8,10–12] but shear-thinning is also often present in frictional or adhesive non-Brownian suspensions[4,5,13–18] or beyond the DST[19]. The spectrum of complex rheological behaviors can also include yielding[6,20,21], normal stress differences (see Guazzelli and Pouliquen[22] for a review), irreversibility under oscillatory shear[23–25], shear-induced microstructure[26], and particle migration[27–32].

To fully understand these complex behaviors, it is essential to consider the direct contact forces between particles. Over the past decade, the crucial role of direct solid contact in governing the flow properties of non-Brownian frictional suspensions has been highlighted by Boyer, Guazzelli, and Pouliquen[33]. They successfully applied a granular paradigm to describe the rheological behavior of dense suspensions of non-Brownian, non-colloidal spheres in a Newtonian fluid, demonstrating the key influence of solid contact interactions induced by particle surface asperities. Using numerical simulations, Gallier *et al.*[9] extensively investigated the effects of asperity height, h_a, and sliding friction coefficient, μ_s, on the rheology of suspensions. Notably, their results showed that μ_s is a key parameter governing the flow properties of frictional suspensions of spheres in the concentrated regime ($\phi > 0.40$). Several numerical studies[7,9,17,31,34,35] have proposed expressions linking the jamming volume fraction to the interparticle friction coefficient. The relationship between ϕ_m and μ_S has paved the way for explaining the rate-dependent rheological behaviors. First, Seto *et al.*[8] and Mari *et al.*[7] demonstrated that the proliferation of frictional contacts is the cause of discontinuous shear-thickening (DST) observed in highly concentrated suspensions of spheres when the shear stress is high enough to overcome the repulsive interparticle forces, leading to direct contact between particles. More recently, Lobry *et al.*[17] and More and Ardekani[36] have numerically shown that the variation of the sliding friction coefficient μ_s with the applied shear stress Σ_{12} can be one of the physical origins of the shear-thinning behavior observed in the

frictional regime. This finding has been corroborated by recent experimental studies, in which the dependence of μ_s on the normal interparticle force –and therefore on Σ_{12}– has been directly measured using Atomic Force Microscopy (AFM)[18,19,37].

Another possible explanation for shear-thinning is the presence of adhesive forces between particles[4,5]. As in the frictional case, the shear-thinning behavior can be quantified by the increase of ϕ_m as Σ_{12} increases. Consequently, $\phi_m(\Sigma_{12})$ can be introduced in Eq. 3 to provide a unified framework for describing both shear-thinning and shear-thickening behaviors in dense suspensions:

$$\eta_s(\phi, \Sigma_{12}) = \left(1 - \frac{\phi}{\phi_m(\Sigma_{12})}\right)^{-2} \tag{4}$$

Shear-induced particle migration in the viscous regime has also been extensively studied in recent decades. The literature reports various migration patterns, including particle migration toward the center of the channel in Poiseuille flow[28,30,32,38], migration toward the outer cylinder in a wide-gap Couette flow[29,39–41], and outward migration in a cone-and-plate geometry[42]. According to the SBM[43] which extended the works from Nott and Brady[44] to the case of curvilinear flows, the particle migration flux is proportional to the divergence of the particle stress tensor Σ^p.

A particular case of migration is the resuspension of particles under the effect of shear flow. Resuspension experiments have been conducted in a vertical Couette geometry where an initially settled layer of particles heavier than the suspending liquid expands upwards when a shear flow is applied[45–47]. Saint-Michel *et al.*[46] and d'Ambrosio, Blanc, and Lemaire[47] measured the vertical particle volume fraction profiles and inferred the particle normal stress in the vorticity direction, Σ^p_{33}, using the Cauchy momentum equation:

$$\frac{\partial \Sigma^p_{33}}{\partial z} = \Delta\rho g \phi \tag{5}$$

Furthermore, Zarraga, Hill, and Leighton Jr[14] demonstrated that the value of Σ^p_{33} could also be deduced from the measurement of the sediment expansion height.

All the aforementioned studies have focussed on suspensions of spherical particles. In contrast, research on non spherical particles remains scarce, and there is still a need for experimental data, as many industrial and natural suspensions consist of non-spherical particles. Mueller, Llewellin, and Mader[48], Hafid *et al.*[49], and Blanc *et al.*[21] demonstrated that the viscosity of concentrated suspensions of faceted particles is significantly higher than that of suspensions of spherical particles, resulting in jamming volume fractions as low as typically 0.45. A few theoretical and experimental studies have investigated the viscosity of suspensions of cubic-like particles in the dilute[50–52]

and semi-dilute[52] regime. The values of K_E and K_B have been found significantly higher than those for suspensions of spherical particles. Mallavajula, Koch, and Archer[50] and Audus *et al.*[51] have numerically determined $K_E \approx 3.1$ for a suspension of cubes. This value has been confirmed by experimental measurements conducted on a suspension of nano-cubes by Mallavajula, Koch, and Archer[50] who found $K_E \approx 3.1$ and on a suspension of micro-cubes by Cwalina, Harrison, and Wagner[52] who founded $K_E \approx 3.5$. Furthermore, Cwalina, Harrison, and Wagner[52] also measured K_B and found a value of 24. In the present paper, we will also determine the values for the coefficients K_E and K_B, and will compare them with previously reported values in the literature.

The present paper describes an experimental study aimed at characterizing the rheological behavior of a viscous, non-Brownian suspension composed of cubic particles, a few hundred microns in size, fabricated using microlithography (Sec. II). Viscosity measurements are performed in the dilute, semi-dilute, and concentrated regimes (Sec. III). The two first regimes are characterized by the values of K_E and K_B which will be compared to those obtained by Mallavajula, Koch, and Archer[50], Audus *et al.*[51], and Cwalina, Harrison, and Wagner[52]. The concentrated regime is characterized by the value of ϕ_m. The last part of the paper (Sec. IV) presents the results obtained on the measurement of the third particle normal stress through resuspension experiments.

II. SUSPENSIONS OF CUBIC PARTICLES

A. Hexahedral particles

The particles, hereafter referred to as cubic, are created using a soft lithography process inspired from[53]. The first step of this process consists in covering a photo-crosslinkable epoxy resin (*SUEX*, *Micro Resist*) dry film, of thickness t_k, with a mask lined with square-shaped holes, of dimensions $a \times a$. The masked films of resin are deposited on a PDMS sheet and then exposed to UV light (*Mercury Light Source Oriel, 350 W, 3 inch*) for a few minutes. The exposure time is approximately proportional to the thickness of the resin, t_k. As will be seen later, we used two film thicknesses: $t_k = 300\,\mu m$ and $t_k \approx 100\,\mu m$ for which the exposure times were set to $240\,s$ and $80\,s$ respectively. After UV exposure, the mask is removed and the film is heated at $T = 65^oC$ for 5 min, followed by heating at $T = 95^oC$ for 10 min.

The development of the exposed resist layers was carried out in propylene glycol monomethyl ether acetate (PGMEA) in order to dissolve the unexposed area of the SUEX film. PGMEA was

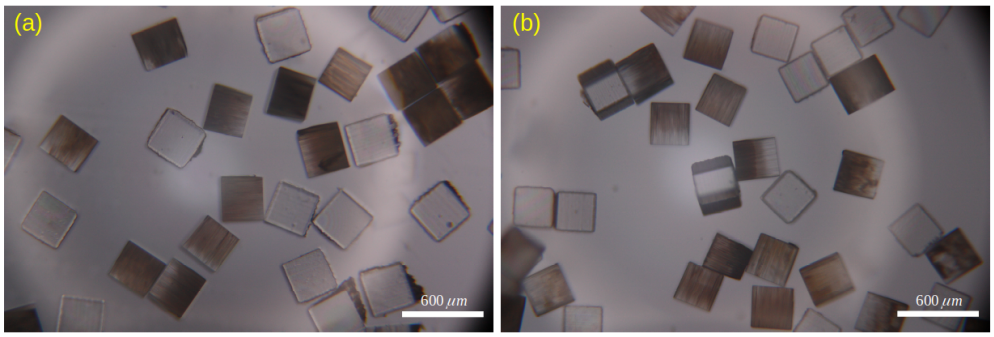

FIG. 1. Examples of cubic particles with $t_k = a \approx 300\mu m$ (a) and hexahedral particles with $t_k \approx 300$ and $a \approx 270\mu m$ (b), imaged with an optical microscope.

then removed by rinsing with ethanol, in order to retain only the solid parts of the resin. After repeating these washing cycles several times, hexahedral particles with dimensions $t_k \times a \times a$ were obtained. The particle density was determined using the volumetric flask method, with the measurement performed in the same fluids as those used for subsequent particle dispersion (see Sec. II B). The measured particle density is $1.19\,g/cm^3$, regardless of the thickness of the film from which they were fabricated. Figure 1 (a) and (b) show examples of such cubic or hexahedral particles with $t_k \approx 300\mu m$ imaged with an optical microscope.

An electron micrograph of the smaller particles ($t_k \approx 100\mu m$) is shown in Fig. 2, where large asperities resulting from the lithographic process can be observed on some faces of the cubic particles. These asperities are even more visible in optical micrographs such as those in Fig. 3. Almost all particles possess four rough faces and two smooth faces. The rough faces exhibit grooves aligned with the direction of UV exposure, likely due to the relatively low spatial resolution of the plastic masks used.

B. Suspensions

The suspensions are then made up of a mixture of cubic ($t_k = a$) and hexahedral particles $t_k \approx 1.1\,a$ or $t_k \approx 0.9\,a$ in order to prevent crystallisation of the suspensions under study. Two types of suspension were studied, depending on the experiments conducted. For the resuspension experiments, particles approximately 300 μm in size were dispersed in a Newtonian mineral oil (*Cargille Laboratories* Serie A, $n = 1.588$), of density $\rho_f = 1.097\,g/cm^3$ (so lighter than the particles) and of viscosity $\eta_0 = 0.103 \pm 0.001\,Pa.s$, measured at $T = 11.5^oC$ which is the work temperature

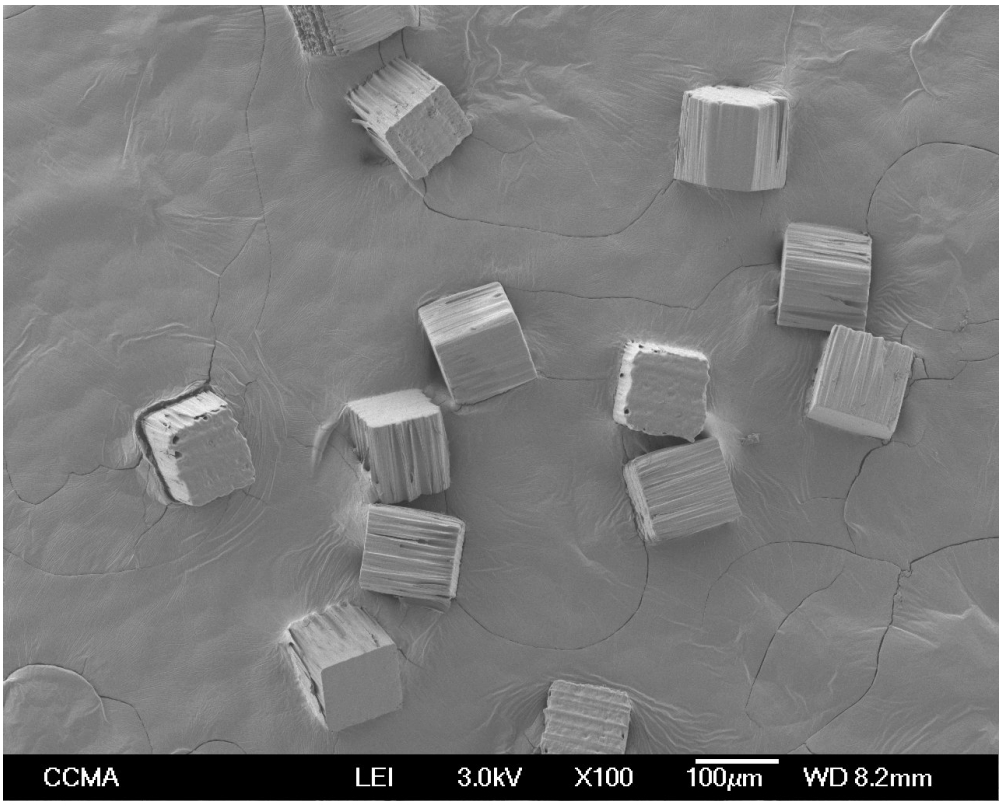

FIG. 2. Examples of cubic particles ($t_k = a \approx 100\mu m$) imaged with an electronic microscope.

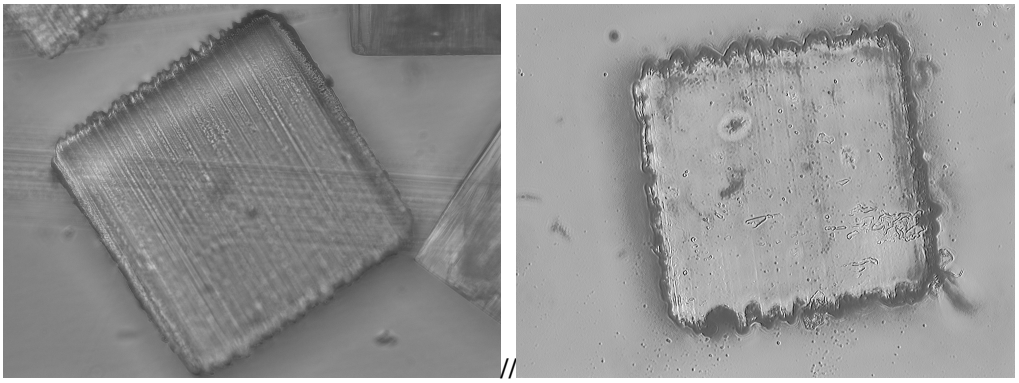

FIG. 3. Examples of cubic particles with $t_k = a \approx 300\mu m$ (left) and $t_k = a \approx 100\mu m$ (right), imaged with an optical microscope.

for the experiments of resuspension. For the conventional rheometric experiments conducted in parallel plate geometry, smaller particles with $a \approx 100\mu m$ were used in order to minimize the apparent wall slip caused by suspension layering near the walls[29,47].These particles are dispersed in another Newtonian mineral oil (*Cargille Laboratories*, Immersion Liquid Code 11295101160) of the same density as the solid particles, $\rho = 1.19\, g/cm^3$, and of viscosity $\eta_0 = (1.055 \pm 0.005)\, Pa.s$,

measured at $T = 21.6^oC$.

Table I summarizes the characteristics of both types of suspensions. Each suspension thus contains hexahedral particles exhibiting variability in both size and shape. This deliberate choice aims to prevent the suspension from undergoing crystallization or from the particles organizing near the confining boundaries. Such phenomena, including crystallization[54,55] and shear banding[29,56], have been reported in monodisperse suspensions of spherical particles and could be expected to occur even more prominently in suspensions of monodisperse cubic particles. Nevertheless, the question arises as to how this variability in particle size and shape influences the rheological behavior of the suspension. While it is difficult to provide a definitive answer, insights can be drawn from studies on suspensions of spheroidal particles. The effect of bidispersity becomes more pronounced as the particle size ratio increases and reaches a maximum for a volume fraction of small particles that depends on the size ratio, but typically lies between 0.3 and 0.5. Wagner and Woutersen[57] investigated the effect of bidispersity in the semi-dilute regime and demonstrated that the Batchelor coefficient decreases from a value of 6 to a minimum of 5.85 (observed for a volume fraction ratio of 0.5) when the particle size ratio is 1.6. In the concentrated regime, numerous studies have investigated the role of bidispersity on the packing density of random assemblies[58] and on the suspension viscosity[59]. These studies consistently show that the viscosity primarily depends on the ratio ϕ/ϕ_m[60], and that for a particle size ratio of 2, the maximum packing fraction ϕ_m varies by only about 2–3%[61]. Therefore, it is likely reasonable to assume that the largest size ratio used in the present study, 1.5, will have a limited influence on the rheological behavior. As for the presence of slightly elongated or flattened particles (with an aspect ratio on the order of 1.1), their influence on the viscosity is expected to be negligible. Based on Jeffery's hydrodynamic calculations, Scheraga[62] computed the intrinsic viscosity of suspensions of spheroids with various aspect ratios and Péclet numbers. They showed that the intrinsic viscosity decreases with increasing Péclet number, and found that for an aspect ratio of 1.2, at zero Péclet number, the intrinsic viscosity was 2.525 for prolate spheroids and 2.524 for oblate ones — both values very close to Einstein's coefficient for suspensions of spherical particles, and expected to be even closer in the non-Brownian regime.

As already mentioned, electron micrographs show the presence of noticeably deep grooves on some faces of the cubes (see Fig. 3). The typical depth of the grooves is approximately $h_c = 7\,\mu m$ and their surface density of about $\zeta_c \approx 0.5$. This high surface roughness on four of the particle faces is problematic in determining the effective solid volume fraction of the suspension. The grooves trap liquid, which, from a hydrodynamic perspective, behaves more like the solid phase.

Experiments	Suspending liquid		Particles	
	density (g/cm^3)	viscosity (Pa.s.)	size (μm)	ratio
Rheometry	1.19	1.055 ± 0.005	100X100X100	(29%)
			110X100X100	(11%)
			150X150X150	(60%)
Resuspension	1.097	0.104 ± 0.005	300X300X300	(66%)
			270X300X300	(34%)

TABLE I. This table lists the compositions of the suspensions used for both viscous resuspension and rheometric experiments.

As a consequence, a correction must be applied to compute an effective particle volume fraction: $\phi^{cor} = \phi^{sol} V^{cor}/V$ where ϕ^{sol} is the solid fraction deduced from the weight fraction of particles, and V^{cor}, the volume of one particle plus the volume of the liquid trapped inside the grooves: $V^{cor} = a^3 (1 + 2\zeta h_c/a)^2$. For the suspension used in the rheometric experiments (40% of the 100 μm particles and 60% of 150 μm particles), the effective volume fractions are found to be 12% higher than the solid concentrations deduced from the particle weight fractions. This leads to a corrected particle volume fraction: $\phi^{cor} = 1.12\ \phi^{sol}$. Note that for the larger cubic particles with a size of about $300\mu m$, the correction is much less important since $\zeta_c \approx 0.4$ and $h_c \approx 5\ \mu m$ leading to ($\phi^{cor} = 1.026\phi$).

In the following, for the sake of simplicity, ϕ will denote the corrected particle volume fraction.

III. VISCOSITY OF SUSPENSIONS OF CUBIC PARTICLES

A. Experimental methods

To prepare the suspensions, a known mass of cubic particles is carefully mixed with a known mass of liquid. The air bubbles are removed by putting the sample in an air vacuum. The suspension is finally gently stirred in order to re-homogenize the particles that would have settled during the degassing procedure and is poured on the lower plate of the rheometer. Rheometric experiments are carried out on a Mars II rheometer (Thermo Fisher Instruments) with an upper rotating parallel plate of radius $R = 40mm$. The upper and lower plates were sandblasted with

$100\,\mu m$ silica beads to increase their roughness and thus reduce possible wall slip and particle layering near the walls. The temperature of the lower disc is controlled and set to $T = 21.6^{o}C$ for all experiments. The gap width is set to $h = 2.5\,mm \approx 17 \times a$.

The choice of a parallel rotating disk geometry is motivated by the negligible shear-induced particle migration in such a geometry, observed for sphere suspensions[41,63]. Although the behavior may differ for suspensions of cubic particles, our experiments show that, after a brief transient phase associated with the adjustment of the microstructure, the apparent viscosity η_{app} remains constant with strain, γ, under a constant shear stress Σ_{12}. This suggests that shear-induced particle migration does not occur.

However, the drawback of this geometry is that the shear rate is not uniform. Specifically, $\dot{\gamma}$ increases from 0 at the center to $\dot{\gamma}_R = \Omega R/h$ at $r = R$, with Ω the angular velocity of the upper rotating plate. In the case of a non-Newtonian behavior, this variation can be problematic since the viscosity, η, depends on the shear rate, $\dot{\gamma}$. To overcome this difficulty and determine the correct viscosity, η, we apply the well-known Mooney-Rabinowitsch correction:

$$\eta = \eta_{app}\left[1 + \frac{1}{4}\frac{\mathrm{d}\ln(\eta_{app})}{\mathrm{d}\ln(\dot{\gamma}_R)}\right] \tag{6}$$

η_{app} is the apparent viscosity given by the rheometer from the measurements of shear rate at the rim of parallel plates, $\dot{\gamma}_R$, and the applied torque, Γ:

$$\eta_{app} = \frac{2}{\pi R^3}\frac{\Gamma}{\dot{\gamma}_R} \tag{7}$$

As shown in the following section, the suspensions under study exhibit relatively weak shear-thinning behavior, and the Mooney–Rabinowitsch correction remains limited—typically on the order of a few percent, and up to 10% for the most concentrated suspension. Another drawback of using a parallel-plate torsional geometry is the occurrence of edge fracture, which can arise when the second normal stress difference, if negative, exceeds a critical threshold—typically on the order of five times the capillary pressure associated with the suspension/air interface[64]. Due to this instability, we were unable to measure the viscosity for shear stresses above $150\,Pa$. Indeed, for the most concentrated suspensions, we observed a deformation of the free surface, which receded and formed an inward-curving meniscus, as soon as the applied stress exceeded—or was close to— $180\,Pa$.

We studied the rheological behavior of suspensions made of cubic particles over a wide range

of shear stress values, $\Sigma_{12} \in [1, 150]\,Pa$, and particle volume fractions, $\phi \in [0.01, 0.31]$.

Within these conditions, the values of the Péclet and Reynolds numbers show that thermal and inertial effects are negligible:

$$Pe = \frac{9}{2}\frac{\Sigma_{12}a^3}{k_BT} > 10^9 \qquad \text{and} \qquad Re = \frac{\rho_f \Sigma_{12} h^2}{\eta_0^2} < 1 \tag{8}$$

At the same time, note that the Stokes number is kept small throughout all the experiments: $St = \left(\frac{1}{18}\right)\frac{\rho_p l_p^2 \Sigma_{12}}{\eta^2} < 10^{-4}$. It is thus expected that only viscous and contact forces govern the rheological behavior of the suspension.

B. Results

Figure 4 shows the variation of the measured relative steady viscosity, $\eta_s = \eta/\eta_0$, with applied shear stress for suspensions made of cubic particles in the dense regime (Fig. 4(a), $\phi \geq 0.17$) and in the semi-dilute regime (Fig. 4(b), $\phi < 0.17$). Each colored point corresponds to an experimental measurement of η_s (relative viscosity corrected using Eq. (6)) at a given ϕ and a given Σ_{12}. The relative uncertainty for each measurement, not shown in Fig. 4 for the sake of clarity, is always smaller than 5%.These results indicate that suspensions of cubic particles exhibit shear-thinning behavior over the explored shear stress range, with the effect becoming more pronounced as ϕ increases. For $\phi \lesssim 0.11$ (see Fig. 4(b)),the suspensions behave almost like a Newtonian fluid.

In this low concentrated regime, the viscosity of suspensions is primarily governed by hydrodynamic forces, with contact interactions between particles being nearly absent or, at most, playing a negligible role. For suspensions of spherical particles, this regime is typically observed for particle volume fractions below 0.25[9,66]. A key consequence of the absence of particle contact interactions is that the rheological behavior is expected to be Newtonian. In Figs. 4, we observed that η_s depends only weakly on Σ_{12} when $\phi \lesssim 0.11$, which thus defines the upper limit below which the suspension can be considered dilute or semi-dilute. As expected, the semi-dilute regime extends over a smaller concentration range for cubic particle suspensions than for spherical particle suspensions. We can define an excluded volume for a cubic particle, corresponding to the total volume it occupies when freely rotating in all directions. This volume is given by the volume of a sphere with a radius equal to $a\sqrt{3}/2$, leading to an effective volume fraction given by

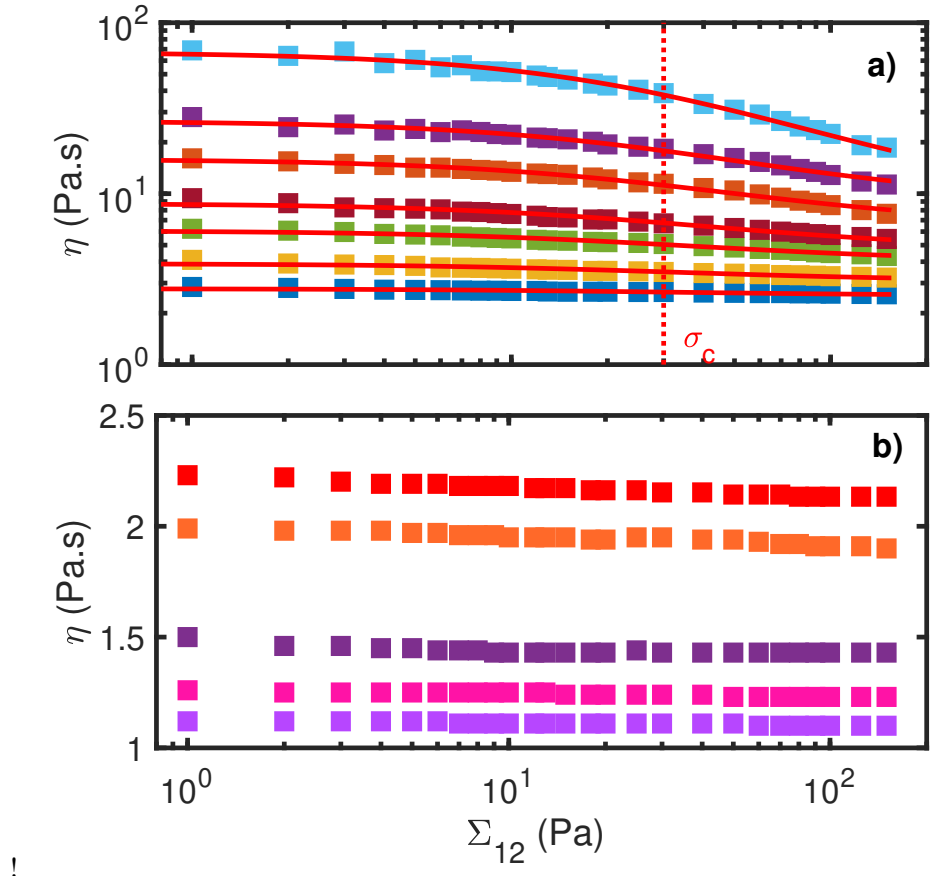

!

FIG. 4. Variation of the shear viscosity η as function of the shear stress Σ_{12} for different values of volume fraction ϕ in (a) the concentrated regime ($\phi \geq 0.14$) and (b) the semi-dilute regime ($\phi \leq 0.112$). The experimental data (colored squares) are fitted by a Krieger-Dougherty model[65] (see Eq. (11)). The values of ϕ are on the bottom graph: 0.011, 0.028, 0.056, 0.084 and 0.112, and 0.140, 0.168, 0.196, 0.224, 0.252, 0.280, and 0.308 on the top graph. At low particle volume fractions (graph b), the suspension exhibits Newtonian behavior. In contrast, at higher concentrations (graph a), a shear-thinning response is observed, characterized by a critical shear stress, σ_C, on the order of several tens of pascals. Notably, this characteristic stress appears to be independent of the cubic particle volume fraction.

$\phi_{eff} = \pi\sqrt{3}/2\ \phi$. Accordingly, the identified limit for the semi-dilute regime, when expressed in terms of ϕ_{eff} is approximately 0.3 – consistent with the threshold established for spherical particle suspensions.

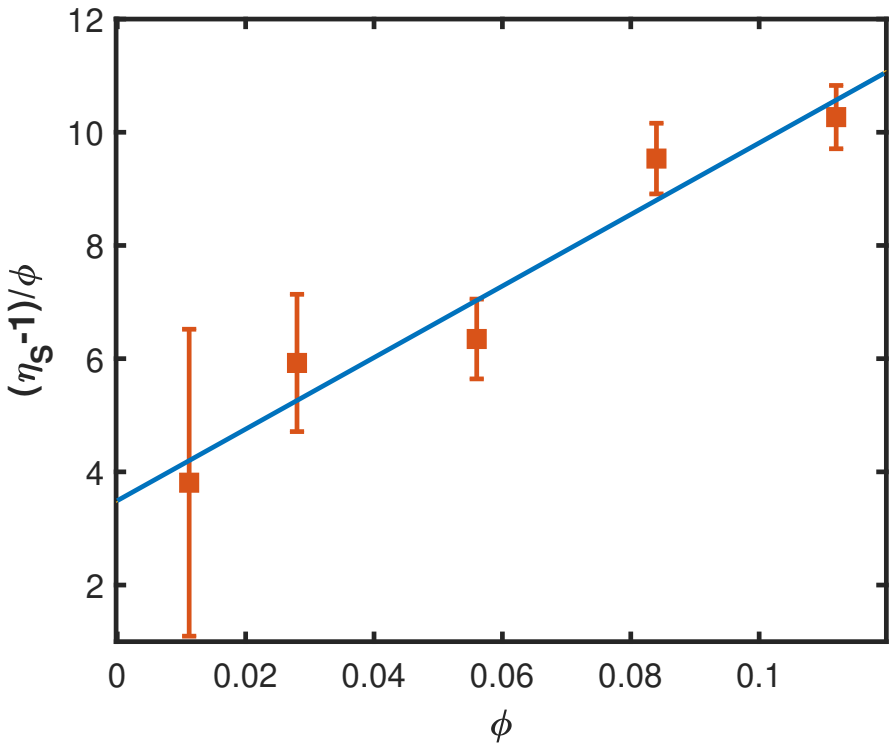

FIG. 5. Variation of the specific viscosity, $\eta_s - 1$, over the volume fraction, ϕ as a function of ϕ in the range $\phi^{\in}[0.011 - 0.11]$). The experimental data (orange squares) correspond to viscosity measurements performed at a shear stress of 50 *Pa*. The data are fitted using Eq. (2) (blue line) yielding fitting parameters $K_E = 3.53$ and $K_B = 62.31$. The fit is performed by assigning a weight to each data point inversely proportional to its uncertainty.

1. The semi-dilute regime

In this regime, the relative viscosity of suspensions can be expressed as an expansion in the particle volume fraction:

$$\eta_S = 1 + K_E\phi + K_B\phi^2 + \mathcal{O}(\phi^3) \tag{9}$$

We recall that K_E and K_B are the Einstein and Batchelor coefficients, respectively. For suspensions of spherical particles, Einstein [1] determined $K_E = 2.5$, and Batchelor [2] demonstrated that K_B depends on the nature of the flow (extensional, Brownian...) and ranges between 5.2 and 7.2. There have been few attempts to evaluate theoretically K_E for cubic particles. Mallavajula, Koch, and Archer [50] computed the intrinsic viscosity for different cube orientations and then averaged the values over all possible orientations. They obtained $K_E = 3.1$ and also demonstrated that the

intrinsic viscosity is sensitive to the roundness of the cube edges – specifically, as the curvature radius increases, K_E decreases. The theoretical value of K_E was experimentally confirmed through measurements on 20 and $100-nm$ Fe_3O_4 nano-cubes dispersed in a low-molar-mass polyethylene glycol and stabilized by oleic acid or PEG brushes. The measured value of K_E was 4.25, but the authors suggested applying a correction to account for the increase in apparent particle size due to the polymer brushes attached to their surface. After this correction, they obtained $K_E = 3.1 \pm 0.2$, in very good agreement with the theoretical value. The theoretical value of K_E was further confirmed by Audus *et al.*[51]. Later, Cwalina *et al.*[52] carried out experiments with cubic aluminosilicate zeolite particles $1\,\mu m$ in size and obtained: $K_E = 3.5 \pm 0.3$ and $K_B = 23.7 \pm 3$ by fitting $(\eta_S - 1)/\phi$ vs. ϕ with $\phi \in [0.023 - 0.137]$:

$$\frac{\eta_s - 1}{\phi} = K_E + K_B\phi \tag{10}$$

Following Cwalina, Harrison, and Wagner[52], we determine K_E and K_B in the semi-dilute regime ($\phi \in [0.011 - 0.11]$) by fitting the variation of $(\eta_S - 1)/\phi$ with ϕ (see Fig. 5). We obtain $K_E = 3.53 \pm 0.4$ and $K_B = 62.31 \pm 5$. The value of K_E is in good agreement with the experimental value reported by Cwalina *et al.*[52]. It is slightly higher than the theoretical value obtained by Mallavajula, Koch, and Archer[50] as well as Audus *et al.*[51], but this value remains within the range of our experimental measurements when error bars are taken into account. As for K_B, the value we measured is significantly higher than that reported by Cwalina et al.[52]. This discrepancy is not unexpected, as the morphology of the particles used in their study differs significantly from ours. While our particles have sharp edges, those used by Cwalina, Harrison, and Wagner[52] are much more rounded.

2. The concentrated regime

In the concentrated regime, the suspensions exhibit clear shear-thinning behavior, which becomes more pronounced as the cubic particle volume fraction increases (Fig. 4). This kind of shear-thinning behavior is commonly observed for non-Brownian suspensions of spherical[13–16] or even faceted (sugar) particles[21]. It is well known that this rheological behavior can have different physical origins depending on the system under study[4,6,13–17,19,21]. In particular, shear-thinning may arise when direct particle contacts occur, a scenario that is promoted by surface

roughness[67,68]. Since our particles exhibit noticeable surface roughness, such contacts are likely to occur. Various contact forces may then contribute to shear-thinning behavior, including adhesive interactions that can potentially lead to particle aggregation. In such a scenario, the suspension would exhibit a yield stress σ_y[69], corresponding to the minimum stress required to break the aggregates formed by these adhesive forces. Above the yield stress, the suspensions would display shear-thinning behavior, as increasing Σ_{12} would progressively break more aggregates, leading to a decrease in viscosity. However, experimental measurements shown in Fig. 4, reveal a Newtonian plateau at large ϕ when $\Sigma_{12} \to 0$, suggesting that adhesive mechanisms are unlikely in the present system. Recent studies literature[17–19,36,37] have shown that variable friction between particles could be another possible physical origin of shear-thinning. In both cases – whether due to adhesive forces between particles or variable friction –, the relevant control parameter is the shear stress, as it governs either the adhesion force between particles or the critical contact force at yield inception, rather than the shear rate. In particular, the characteristic shear stress associated with shear-thinning behavior is expected to be independent of the particle volume fraction.

This feature is consistent with the variation of viscosity with shear stress, as shown in Fig. 4, where the characteristic shear stress associated with shear-thinning is on the order of a few tens of pascals, regardless of the volume fraction of cubic particles. The decrease in viscosity is well captured by the model originally proposed by Krieger and Dougherty[65] to account for the shear-thinning behavior observed in suspensions of Brownian particles:

$$\eta = \eta_\infty + \frac{\eta_0 - \eta_\infty}{1 + \frac{\Sigma_{12}}{\sigma_c}} \tag{11}$$

where η_0 and η_∞ are the high- and low-shear limiting viscosities, respectively, and σ_c is the characteristic shear stress, which characterizes shear-thinning. The red lines in Fig. 4 represent the best fit to the viscosity decrease with $\sigma_c = 30\ Pa$. Notably, Krieger and Dougherty[65] showed that, for colloidal dispersions, the characteristic stress, σ_c, is independent of particle concentration. The same is expected for non-Brownian suspensions, where shear-thinning arises from either adhesive forces or variable friction. In the first case, the stress scale is set by the adhesive force between particles ($\sigma_c \approx F_{adh}/(6\pi a^2)$) and, in the second case, by the critical force, L_C, at which particle contacts enter the plastic regime ($\sigma_c \approx L_C/(6\pi a^2)$)[17], regardless of the particle volume fraction. For this reason, we assume σ_c to be constant for all particle volume fractions. The values of the

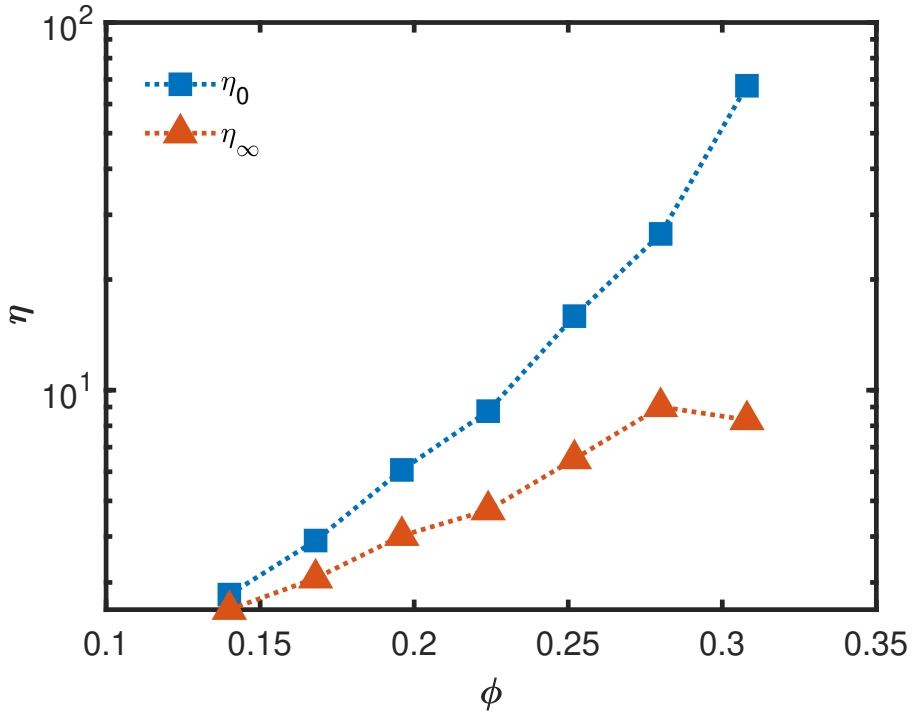

FIG. 6. Variation of high- and low-shear limiting relative viscosities, η_0 and η_∞ as a function of the solid volume fraction ($\phi \in [0.01, 0.31]$) for the suspensions made of cubic particles. σ_c is set to 30 *Pa* for all particle volume fractions.

two other free parameters, η_0 and η_∞ are displayed as functions of ϕ in Fig. 6.

Shear-thinning can also be captured—in a more compact form—by introducing a stress-dependent jamming volume fraction, $\phi_m(\Sigma_{12})$[17,21,70–72]. Figure 7(a) displays the evolution of η_s with ϕ for six different values of Σ_{12}. The experimental data, displayed as colored squares, are well captured by a modified Maron-Pierce law (coloured lines):

$$\eta_s = \frac{\alpha(\Sigma_{12})}{\left(1 - \dfrac{\phi}{\phi_m(\Sigma_{12})}\right)^{-2}} \tag{12}$$

As previously explained, introducing a stress-dependent jamming fraction allows for an effective description of the shear-thinning behavior. The introduction of the parameter α is not strictly necessary, but it improves the fit quality. As we will see later, its value is close to 1, which is the expected value at low volume fractions. Furthermore rather than directly fitting the viscosity variation with particle volume fraction, we chose to fit the inverse of the square root of the viscosity

as a function of ϕ to assign a more balanced weight to each measurement performed at different concentrations (see Fig. 7(b)). However, we verified that directly fitting the viscosity as a function of ϕ does not significantly change the results. The resulting values of α and ϕ_m and their variations with Σ_{12} are shown in Fig. 8.

As expected, we observe that ϕ_m increases with Σ_{12}, which illustrates the shear-thinning behavior. Specifically, ϕ_m ranges approximately from 0.35 at $\Sigma_{12} = 1\,Pa$ to 0.41 at $\Sigma_{12} = 150\,Pa$. These values are significantly smaller than those observed for non-Brownian suspensions of spherical particles, where $\phi_m \in [0.54, 0.66]$ (see, for instance,[22] for a review). These low values of ϕ_m for non-spherical particle suspensions align well with the experimental findings of Blanc *et al.*[21] who reported ϕ_m values between 0.43 and 0.50 for suspensions of single-sized faceted (i.e. irregular polyhedrons) sugar particles (with a size of approximately $100\,\mu m$) suspended in a Newtonian oil and sheared within the same range of Σ_{12} as in the present study.

3. Discussion on the extremely high viscosity for suspensions of cubic particles

Since the numerical studies of Mari *et al.*[7] and Gallier *et al.*[9], it has been well-known that the jamming volume fraction, ϕ_m, is strongly dependent on the sliding friction coefficient, μ_s. Numerical studies on spherical particles consistently show that as the friction coefficient μ increases from 0 to ∞, the jamming volume fraction ϕ_m decreases from values in the range of 0.63 to 0.68 down to a typical value of approximately 0.55[7,8,17,35]. Therefore, sliding friction alone cannot account for the very low values of ϕ_m that we have measured for suspensions of cubic particles. Moreover, studies on dry granular media[73,74] and suspensions[75,76] have shown that rheology is highly sensitive to rolling friction between particles and that accounting for rolling resistance allows for an accurate description of the rheology of granular media or suspensions composed of faceted particles. The numerical simulations of Estrada *et al.*[74] on granular media have shown that the resistance to rolling motion induced by a non-spherical shape can be effectively modeled by approximating the non-spherical particles as a spheres 'equipped' with an apparent rolling resistance torque characterized by a rolling friction coefficient, μ_r.

Singh *et al.*[75] studied, through numerical simulations, the influence of a rolling constraint on the emergence of discontinuous shear thickening (DST) and, more generally, on the rheology of suspensions of frictional, non-Brownian spheres. The rolling constraint can arise from the shape

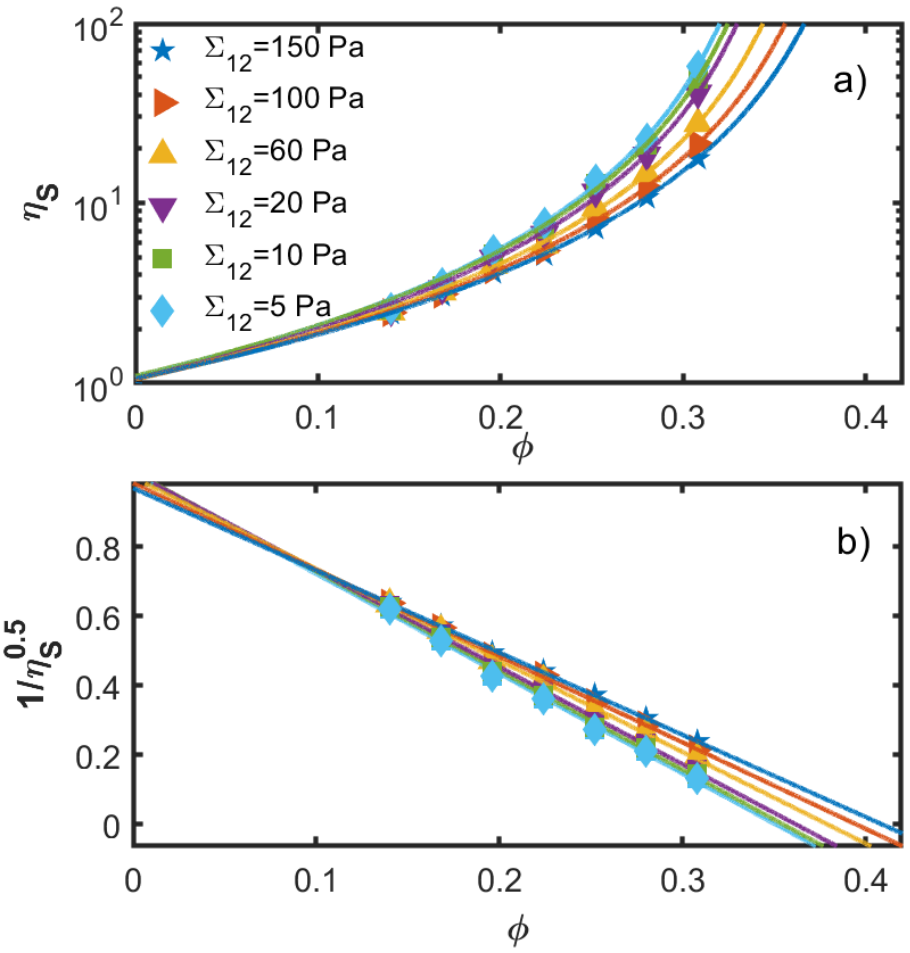

FIG. 7. (a) Relative shear viscosity, η_s, as a function of the particle volume fraction, ϕ, for six different applied shear stresses, $\Sigma_{12} \in [5, 150]$, Pa. (b) Inverse square root of the shear viscosity as a function of ϕ. The experimental data (colored squares) are fitted using Eq. (4). The resulting fitting parameters, α_0 and ϕ_m, are reported in Fig. 8.

of the particles[76] or the presence of adhesive forces[5]. Singh *et al.*[75] provided a comprehensive study of the influence of both the sliding and rolling friction coefficients (μ_S and μ_r, respectively) on the viscosity of suspensions. They summarized this influence by examining the dependence of the jamming fraction on μ_S and μ_r (see Fig. 9, which illustrates their results).

Interestingly, Singh *et al.*[75] demonstrated that ϕ_m depends weakly on μ_r when μ_S is sufficiently small (typically, $\mu_S \lesssim 0.35$) but exhibits a strong dependence on μ_r when $\mu_S \gtrsim 0.5$. For instance, over the same range of rolling friction coefficients ($\mu_r \in [10^{-3}, 10]$), the authors showed that for $\mu_S = 10$, ϕ_m decreases from 0.57 to 0.36 as μ_r increases from 10^{-3} to 10 (see the purple curve in

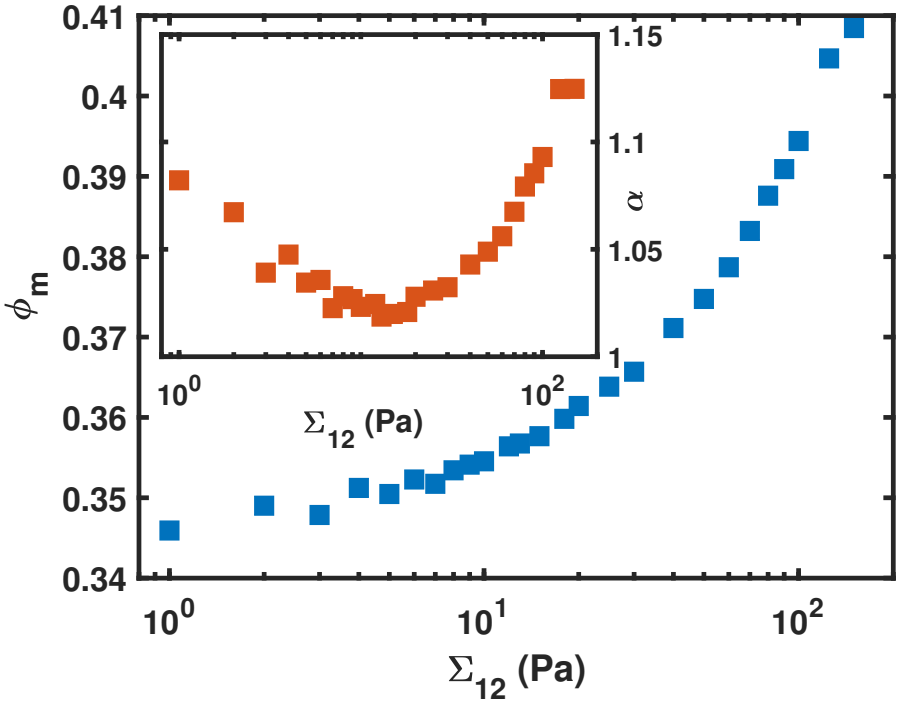

FIG. 8. Variation of the jamming volume fraction, ϕ_m, obtained by fitting $1/\eta_s^{0.5}$ as a function of the particle volume fraction, ϕ, and plotted against the applied shear stress, Σ_{12}. The inset shows the corresponding values of the fitting parameter α, which remain close to 1, as expected.

Fig. 9). Note that this finding is consistent with the results obtained by Benmebarek and Movahedi Rad [78] regarding the effect of rolling resistance on the shear properties of granular media. In particular, they showed that for particles with a low to moderate sliding friction coefficient, the rolling resistance coefficient has a marginal effect on shear stress and volume change during the shearing process, whereas this effect is significant for grains with a high sliding resistance.

Returning to suspensions, the low values of ϕ_m obtained for high sliding and rolling friction coefficients are in good qualitative agreement with our experimental results. Following Estrada, Taboada, and Radjai [73], Estrada *et al.* [74] and d'Ambrosio, Koch, and Hormozi [76], for cubic particles, the rolling friction coefficient can be estimated to be on the order of $1/2$. For this value of μ_r, the numerical results of Singh—obtained, it should be noted, for suspensions of spherical particles—show that the jamming volume fraction can decrease to values as low as approximately 0.44, which approaches the range of jamming volume fractions measured in our experiments with cubic particle suspensions. Attempting to further reconcile the experimental results presented here with Singh's numerical results would not be particularly meaningful. Estrada and collaborators

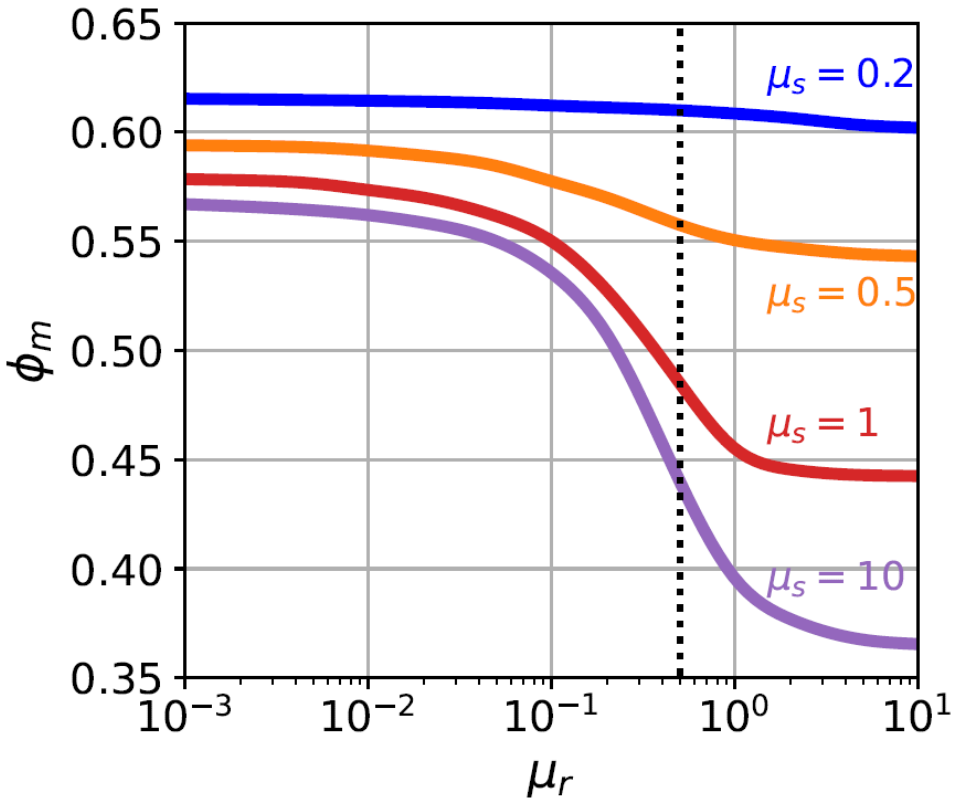

FIG. 9. The jamming volume fraction ϕ_m as function of sliding friction coefficient, μ_s, and rolling friction coefficient, μ_r, as computed by Singh *et al.*[75,77]. The corresponding dataset is available at: `https://acdc.alcf.anl.gov/mdf/detail/singh_rolling_friction_prl_2020_v1.4/`.

have shown that representing polygons as disks with an imposed rolling resistance is only truly relevant when the number of polygon sides is sufficiently large. Moreover, it is quite evident that hydrodynamic forces, particularly lubrication forces, differ significantly between spherical and cubic particles. Thus, even if we were able to provide a realistic and precise value for the rolling friction coefficient, applying Singh's numerical results—obtained for spheres under a rolling constraint—to our findings would not be particularly meaningful or physically justified.

To conclude this discussion, both sliding friction and shape-induced rolling friction clearly play a significant role in the low values of ϕ_m (i.e., the high viscosity) observed in suspensions of cubic particles. Our results are in qualitative agreement with the numerical findings of[75,77] on the rheology of suspensions of spherical particles subjected to a rolling constraint in addition to the more widely studied sliding constraint. However, it is unrealistic to expect that the rheology of suspen-

sions of cubic particles can be accurately modeled by replacing them with spheres incorporating rolling friction. In particular, hydrodynamic interactions are known to be significantly different, as already observed in the dilute and semi-dilute regimes, where we have determined Einstein and Batchelor coefficients that differ substantially from the well-established values for spheres.

C. Shear reversal experiments

Shear reversal experiments have been shown to be a valuable tool for assessing the role of direct contact forces in the viscosity of suspensions of spherical particles[21,79]. In such experiments, when the flow direction is reversed, the viscosity drops abruptly, reaches a minimum, and then increases again to the value it had before the shear reversal. It has been shown that the minimum viscosity, η_{min}, is primarily related to the contribution of hydrodynamic interactions between particles, while the difference between the steady-state viscosity and the viscosity at the minimum, $\Delta\eta_S$, provides an estimate of the contribution arising from direct particle contacts[79,80]. Shear reversal experiments have also been applied to suspensions of faceted particles, revealing the emergence of a master curve when the difference between the steady and minimum viscosity, normalized by the steady viscosity, is plotted against the ratio ϕ/ϕ_m[21]. Figure 10 shows the transient viscodity responses obtained for suspensions of cubic particles at different particle volume fractions. Our findings indicate that, unlike rigid spherical suspensions -where shear reversal effects are typically observed at volume fractions above 0.30–0.35- cubic suspensions exhibit a measurable transient viscosity response even at much lower volume fractions, down to 0.14. Additionally, we note that for lower particle volume fractions, no transient response is observable. This critical volume fraction, above which shear transients are detected, is entirely consistent with the threshold we previously determined for distinguishing the dilute or semi-dilute regimes—where the behavior remains nearly Newtonian—from the concentrated regime, where shear-thinning behavior is observed.

Figures 11 (a) and (b) show the variations of η_{min} and $\Delta\eta_S$ with Σ_{12}. We can observe that η_{min} remains almost constant with respect to Σ_{12} whereas $\Delta\eta_S$ decreases significantly as Σ_{12} increases. This is supplementary evidence that the shear-thinning behavior observed in Fig. 4 originates from contact interactions between particles.

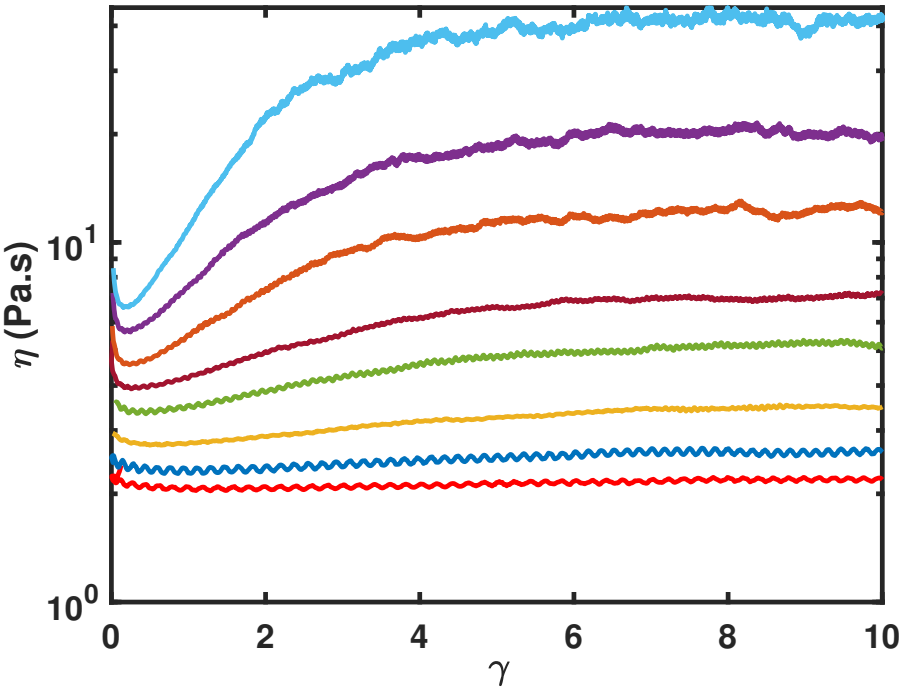

FIG. 10. Transient response during shear reversal experiments for suspensions of cubic particles at various volume fractions, measured under an applied shear stress of $\Sigma_{12} = 20, \mathrm{Pa}$. The transient viscosity is plotted as a function of the strain accumulated following the reversal of the flow direction. Different colors indicate different particle volume fractions, using the same color scheme as in Fig. 4 (ϕ =0.112, 0.140, 0.168, 0.196, 0.224, 0.252, 0.280, and 0.308 from bottom to top).

IV. VISCOUS RESUSPENSION EXPERIMENTS

A. Viscous resuspension and particle normal stresses

As mentioned in the introduction, Zarraga, Hill, and Leighton Jr [14] demonstrated that the particle normal stress in the vorticity direction can be evaluated by measuring the expansion of a sediment sheared in a vertical cylindrical Couette geometry. To this aim, they revisited the experimental results of Acrivos, Mauri, and Fan [45] who studied the resuspension of various suspensions made of different spherical particles in a vertical narrow-gap Couette device, demonstrating that the relative expansion of the sediment $(h_s - h_0)/h_0$ was governed by the Shields number, Sh:

$$\frac{h_s - h_0}{h_0} = f(Sh) \qquad \text{with} \qquad Sh = \frac{9}{2}\frac{\eta_0 \dot{\gamma}}{\Delta\rho g h_0} \tag{13}$$

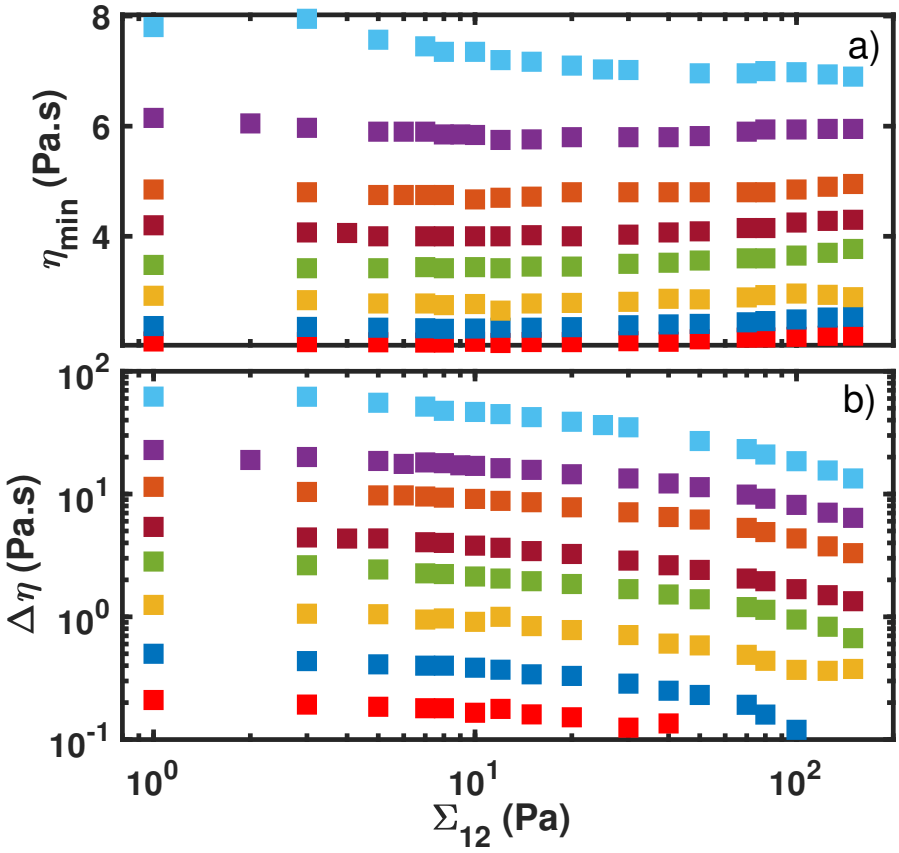

FIG. 11. (a) variation of the viscosity at the minimum with respect to Σ_{12}. (b) variation of the difference of the steady and minimum viscosity with respect to Σ_{12}. The different colors represent various particle volume fractions, using the same color scheme as in Fig. 4 (ϕ =0.112, 0.140, 0.168, 0.196, 0.224, 0.252, 0.280, and 0.308 from bottom to top).

h_0 and h_s being the initial sediment height and the height of the expanded sediment, respectively.

From the momentum balance equation (Eq. 5) and using the conservation of particle number, Zarraga, Hill, and Leighton Jr [14] obtained the following equations linking the particle normal stress to the particle concentration at the bottom of the particle bed, $\phi(0)$:

$$\left[\frac{\Sigma^p_{33}}{\eta_0\dot{\gamma}}\right]_{\phi(0)} = (\lambda_3\eta_n)|_{\phi(0)} = \frac{9\phi_0}{2\,Sh} \tag{14}$$

and

$$\phi(0) = \frac{h_0\phi_0}{h_s - d\,h_s/d\ln(Sh)} \tag{15}$$

where ϕ_0 is the particle volume fraction of the sediment.

Therefore, using eqs.(14) and (15), Σ_{33}^{p} can be determined by measuring the resuspension height for various Shields numbers.

Using the experimental results of Acrivos, Mauri, and Fan[45], Zarraga, Hill, and Leighton Jr[14] demonstrated that the expansion of the settled bed can be described by the following equation:

$$h_s/h_0 = 1 + C \times Sh^n \qquad \text{with} \qquad C = 0.66 \qquad \text{and} \qquad n = 1/3 \tag{16}$$

Then, from Eqs. (14-16), it is straightforward to deduce the variation of the third particle normal stress, Σ_{33}^{p}, normalized by $\eta_0\dot{\gamma}$, by knowing ϕ_0 and $\phi(0)$:

$$\lambda_3\eta_n(\phi(0)) = \frac{9\phi_0}{2}\left(\frac{2C}{3}\right)^3\left(\frac{\phi(0)}{\phi_0-\phi(0)}\right)^3 \tag{17}$$

By assuming $\phi_0 \approx \phi_m \approx 0.62$ and defining $K_Z = (9\phi_m/2)(2C/3\phi_m)^3$, Zarraga, Hill, and Leighton Jr[14] obtained finally the simple expression:

$$\lambda_3\eta_n(\phi) = K_Z\left(\frac{\phi}{1-\phi/\phi_m}\right)^3 \text{ with } K_z \approx 1 \tag{18}$$

B. Experimental methods

1. Device

The experimental device is the same as that used in previous works[47,81]. The suspension is sheared in a vertical Couette cell, $10\,cm$ high, made of PMMA mounted on a controlled-stress rheometer (*Mars II Thermofisher*) (see Fig. 12(a)). The inner cylinder has a radius of $R_1 = 19\,mm$ and rotates at a constant angular velocity, Ω, while the outer cylinder (stator) has a radius of $R_2 = 24\,mm$. In this configuration, the gap is much larger than the particle size ($(R_2-R_1)/l_p \approx 17$), which should limit particle layering and wall slip effects often observed in non-Brownian suspension flows[29]. However, a drawback of using such a wide-gap geometry is that the shear stress in the gap is not uniform but varies as $1/r^2$, where r ranges from R_1 to R_2. Consequently, the shear stress varies by a factor of 1.6 across the gap, potentially leading to radial shear-induced particle migration.

Despite this flow heterogeneity and the fact that the suspension is not perfectly Newtonian (see Sec. III), we will nonetheless define a macroscopic shear rate based on the value expected at the

center of the gap for a Newtonian fluid:

$$\dot{\gamma} = \frac{4R_2^2 R_1^2}{\left(R_2^2 - R_1^2\right)\left(R_1 + R_2\right)^2}\Omega \tag{19}$$

The angular velocity of the rotor is varied from 0.5 to $60\,rpm$, ensuring that both Brownian motion and inertial effects can be neglected. The Peclét number ($Pe = 6\pi\eta\dot{\gamma}a^3/(k_B T)$) remains higher than 10^9 while the Reynolds number ($Re = \rho\Omega R_1\left(R_2 - R_1\right)/\eta$) stays below 0.6. The bottom of the Couette cell is first filled with mercury in order to prevent particle migration toward the region located under the rotor and to enhance slip at the bottom, thereby promoting a more homogeneous shear rate in the vertical direction[45,82]. The suspension is then poured into the cup, and the rotor is slowly moved down until it dips into the mercury, maintaining a distance of approximately $2\,mm$ from the cup bottom.

A fluorochrome (*Nil Blue A*) is dissolved in the suspending liquid. When the particles are added to the suspending liquid, we observe that Nil Blue A adsorbs onto their surface, making them fluorescent when illuminated. As we will see later, this fluorescence facilitates the detection of the interface between the suspension and the clear fluid. A thin vertical laser sheet (thickness $\approx 50\,\mu m$), offset by $y_0 = 17\,mm$ from the radial plane (see Fig. 12(b)) is used to illuminate the suspension, while a camera (*IDS UI-3290SE-M-GL*) is positioned at 90° to the enlightened plane. Initially, the goal of this study was to observe individual cubic particles and perform local measurements of concentration and velocity, similar to our previous work on suspensions of spherical particles[47,81]. However, poor refractive index matching prevented the individual detection of solid particles. This mismatch is likely due to the intrinsic heterogeneity of the cubic particles themselves, which, as seen in Fig. 3, exhibit holes and surface asperities likely not fully filled by the suspending liquid.

Nevertheless, the lighting of the suspension by the laser sheet, coupled with the fluorescence of the particles and the resolution of the camera allows for the acquisition of images with a clear view of the sharp front separating the suspension from the clear fluid (see Fig. 13).

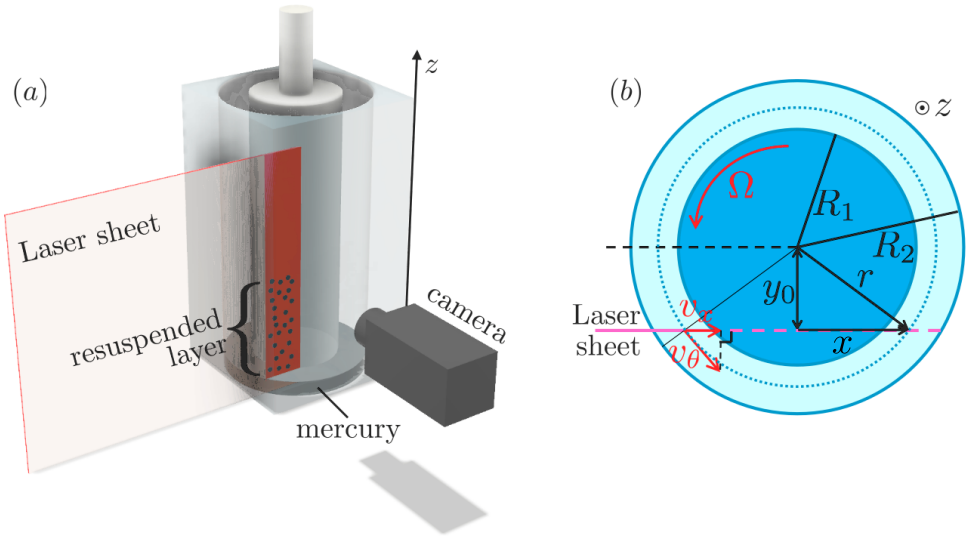

FIG. 12. a) Sketch of the experimental device used to study the viscous resuspension of cubic particles. b) View from above. The vertical laser sheet is shifted by a distance $y_0 < R_1$ from the radial plane (dashed black line). x is the horizontal position in the laser sheet and z is the vertical position. $z = 0$ is set by the mercury/suspension interface.

2. *Measurements methods*

To conduct the viscous resuspension experiments, the rotor angular velocity Ω is initially set to 5 rpm for a period before being adjusted to the desired value, ranging from 0.5 to 60 rpm. The torque Γ is continuously recorded throughout the experiments, and steady state is considered reached once Γ stabilizes (corresponding to a transient time of about 1000 s). At this point, 10,000 images of the resuspended suspension are captured and averaged into a single frame. Figure 13 presents an example of the initial sediment (extreme left frame) along with five examples of the resulting averaged frames at different imposed rotor angular velocities (Ω, increasing from left to right). In each averaged image, the rotor is positioned on the right side, while the stator is on the left. As expected, a clear increase in the resuspended suspension height, h_s, is observed as the rotor angular velocity Ω increases.

To determine the suspension height for each rotor angular velocity , we measured the light intensity horizontally averaged across a centered region of the gap in the frame obtained from the average of 10,000 images captured during the resuspension experiments (except for the sediment, where only a few images were captured due to the long settling time of the cubes). We

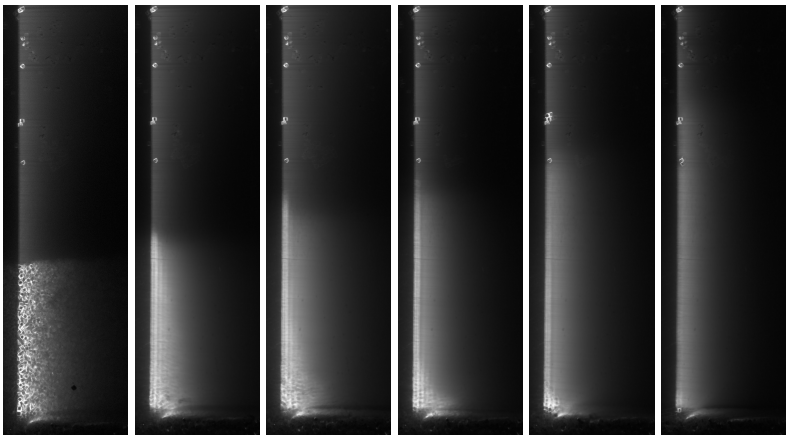

FIG. 13. From left to right: sediment ($\Omega = 0\,rpm$); images resulting from an average of the 10000 captured images for different values of the rotor angular velocity: $\Omega = 0.5\,rpm$; $\Omega = 2\,rpm$; $\Omega = 5\,rpm$; $\Omega = 20\,rpm$; $\Omega = 60\,rpm$. For each image, the rotor (inner cylinder, $R_1 = 19\,mm$) is on the right while the stator (outer wall, $R_2 = 24\,mm$) is on the left. Scale: $e \approx 65\,px/mm$. Gap size on each frame $\approx 8.46\,mm$ (laser offset: $\Delta y \approx 17.0\,mm$).

chose to exclude the regions near the walls when measuring h_s due to the presence of a meniscus at the interface with the mercury layer which makes it difficult to properly define the bottom of the suspension. Note that Fig. 13 clearly shows the meniscus formed near the stator wall in the bottom-left area of each frame. A similar meniscus is assumed to be present on the rotor side, even though it is not directly observable. It should also be noted that the interface between the suspension and the clear fluid is not perfectly horizontal. This inclination is likely due to a slight misalignment of the rotor with respect to the stator, despite our efforts to minimize it as much as possible. A similar inclined interface was observed by Saint-Michel *et al.* [46] who investigated the resuspension of spherical particles in a narrow-gap Couette geometry. Their results were later analyzed numerically by Badia *et al.* [83], who showed that a small eccentricity between the cylinders (5% in their numerical study) could lead to an inclined interface between the suspension and the clear fluid. Badia *et al.* [83] also evaluated the impact of such eccentricity on the measurement of Σ^p_{33}, concluding that for small eccentricities, the effect on the measurement of the particle stress is significant only at low volume fractions or high Shields numbers ($Sh \gtrsim 10$). Our results should therefore be only marginally affected by this slight misalignment.

Figure 14 presents a photograph of the sediment (top) along with the corresponding light intensity measurement (bottom). Similarly, Figures 15 and 16 display the averaged frame from

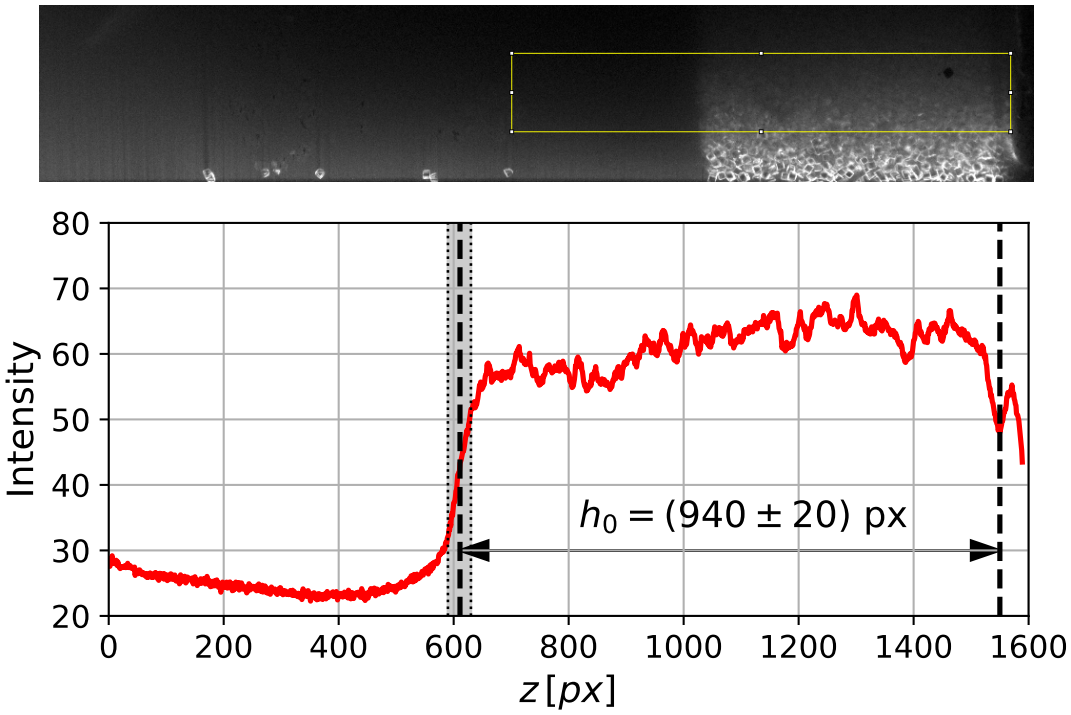

FIG. 14. **Top**: Sediment picture in the Couette gap. The yellow frame corresponds to the intensity measurement area. **Bottom**: Intensity variation (red line) measured as function of the height $z\,[px]$. The sediment height is determined between the two vertical dashed lines: $h_0 = (940 \pm 20)\,px$.

the 10,000 captured images (top) and the corresponding light intensity variation (bottom) for $\Omega = 0.5$ rpm and $\Omega = 2$ rpm, respectively. The sharp variation in light intensity allows for accurate localization of the suspension bottom position, $z(0)$. The location of the suspension/clear fluid interface, $z(h_s)$, is determined at the inflection point of the light intensity profile (see Figs. 14, 15 and 16), which allows the determination of the resuspension height, $h_s = z(h_s) - z(0)$. Tab. II presents the various measurements of h_s versus rotor angular velocity.

C. Results

1. Resuspended suspension height

Figure 17 shows the variation of the resuspended height difference, $h_s - h_0$, normalized by the sediment height, h_0, as a function of the macroscopic Shields number, Sh, defined by[45] (Eq. 13)

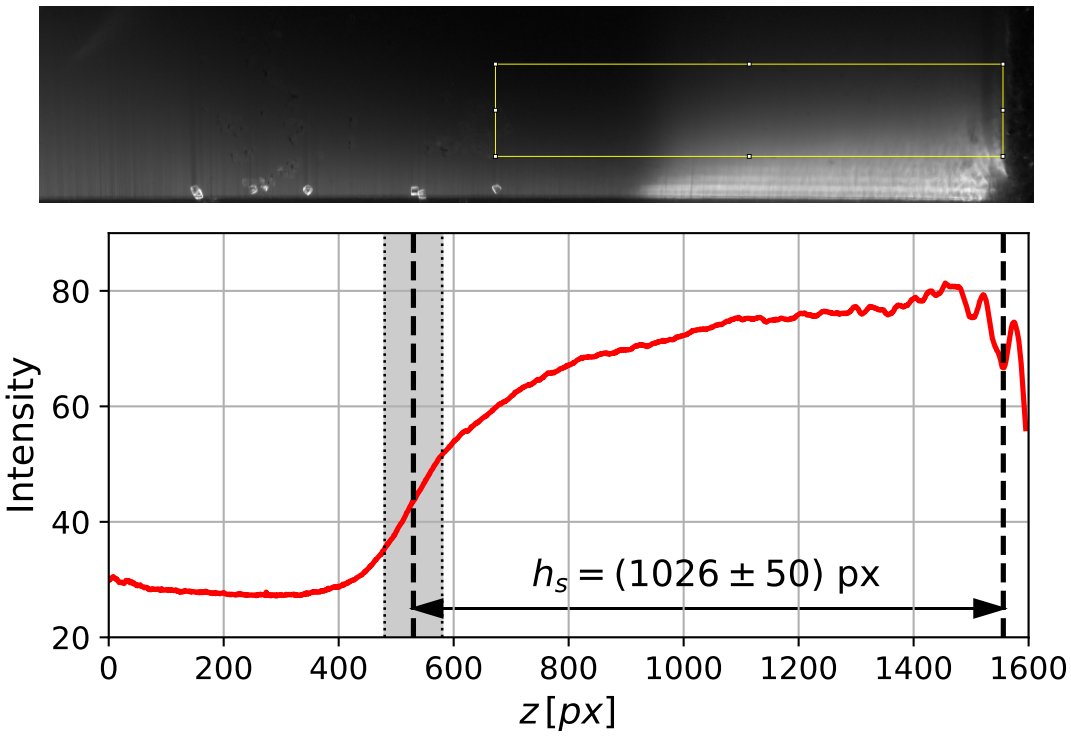

FIG. 15. **Top**: Averaged frame in the Couette gap for $\Omega = 0.5\,rpm$. The yellow frame corresponds to the intensity measurement area. **Bottom**: Intensity variation (red line) measured as function of the height $z\,[px]$. The suspension height is determined between the two vertical dashed lines: $h_s|_{\Omega=0.5\,rpm} = (1026 \pm 50)\,px$.

Ω [rpm]	0	0.5	1	2	5	10	20	30	40	60
h_s [mm]	14.6	15.8	16.8	18.3	20.6	22.3	24.0	25.7	27.7	28.7
Δh_s [mm]	0.3	0.8	0.8	0.8	0.8	0.8	0.8	0.8	1.1	0.8

TABLE II. Table gathering the different measured values of suspension height h_s and uncertainties Δh_s for all the imposed rotor angular velocities Ω.

In the experiments, $\dot{\gamma}$ ranges from 10^{-1} to $13\,s^{-1}$, and then the Shields number Sh varies from 4×10^{-3} to 0.5. It should be noted that, according to the literature[47,84], the true shear rate inside the Couette gap is probably lower than the apparent one deduced from Eq. (19). It is therefore likely that the values of the Shields number are slightly under-estimated.

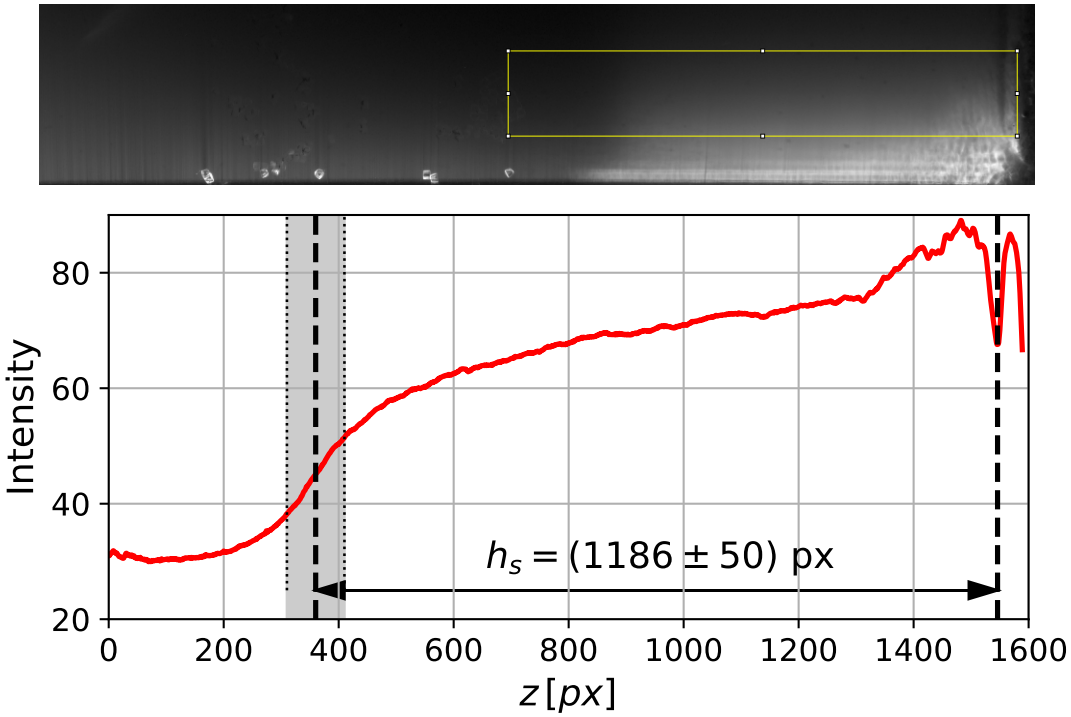

FIG. 16. **Top**: Averaged frame in the Couette gap for $\Omega = 2\,rpm$. The yellow frame corresponds to the intensity measurement area. **Bottom**: Intensity variation (red line) measured as function of the height $z\,[px]$. The suspension height is determined between the two vertical dashed lines: $h_s|_{\Omega=2\,rpm} = (1186 \pm 50)\,px$.

In Fig. 17, as expected, the re-suspended suspension height h_s increases with increasing Sh. The experimental data (blue squares) are fitted with a function of the same type as that proposed by Zarraga, Hill, and Leighton Jr [14] to describe the viscous resuspension of spherical particles:

$$h_s/h_0 = 1 + C \times Sh^n \tag{20}$$

We recall that Zarraga, Hill, and Leighton Jr [14] determined $C \approx 0.66$ and $n = 1/3$ for non-Brownian suspensions of spherical particles, based on the experimental work of Acrivos, Mauri, and Fan [45]. For comparison, this variation is plotted as a solid red line in Fig. 17, along with the fits to our data obtained either by treating n as a free parameter (orange dotted line) or by fixing its value at 1/3 (green dashed line). Interestingly, the experimental data for cubic particles are well described by Eq. (20) with the same exponent value n as for spheres ($n \approx 1/3$), while the coefficient C is roughly twice as large as that found for spherical particles. At a fixed Shields number, viscous resuspension appears to be more efficient for cubic particles than for spheres. This suggests that particle normal stresses, Σ^p_{ii},are higher in suspensions of cubic particles than in those of spherical particles, for

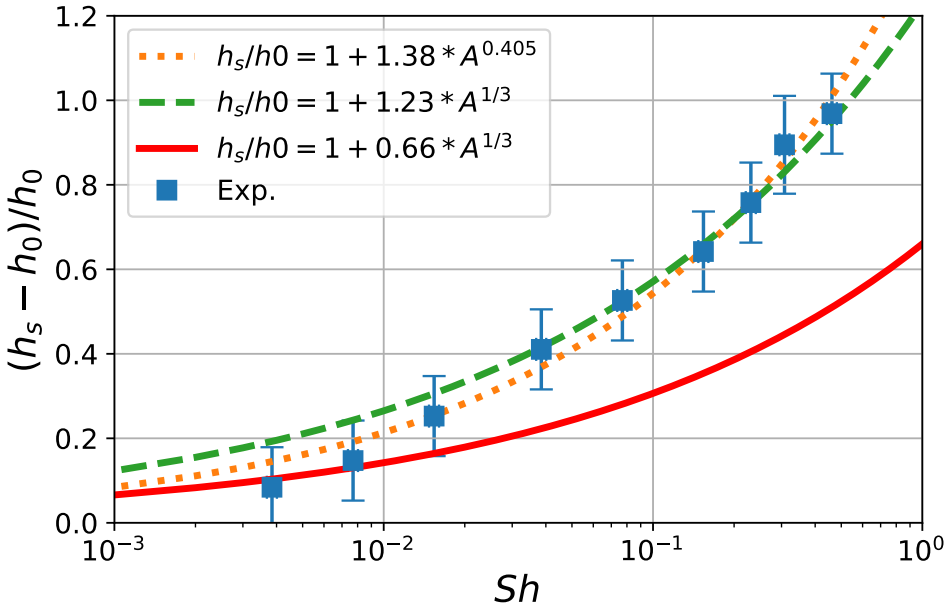

FIG. 17. Variation of the normalized resuspension height, $(h_s - h_0)/h_0$, as a function of the macroscopic Shields number, $Sh = \frac{9\eta_0\dot{\gamma}}{2\Delta\rho g h_0}$. Experimental data (blue squares) are fitted using a power-law model: $y = Cx^n$. The orange dotted line shows the best fit with both C and n as fitting parameters, while the green dashed line represents the best fit with n fixed at $1/3$. For comparison, the resuspension trend reported by Zarraga, Hill, and Leighton Jr [14], based on the experimental data of Acrivos, Mauri, and Fan [45] for viscous resuspension of spherical particle suspensions, is also shown (red line).

a given particle volume fraction and Shields number (or equivalently for a given shear rate $\dot{\gamma}$). This observation aligns with previous rheological studies[21,49,52], which report that suspensions of faceted particles exhibit higher viscosity than those of spheres at the same volume fraction ϕ and shear rate. Our own rheometric measurements, presented in Sec. III, further support this trend, confirming that suspensions of cubic particles consistently display higher viscosity compared to suspensions of spherical particles.

2. *Concentration at the bottom*

As explained before, referring to the work of Zarraga, Hill, and Leighton Jr [14], the volume fraction at the bottom of the suspension ($\phi(0) = \phi(z = 0)$) can be deduced from the measurements of the resuspension height, h_s and the knowledge of the solid fraction in the sediment (in absence

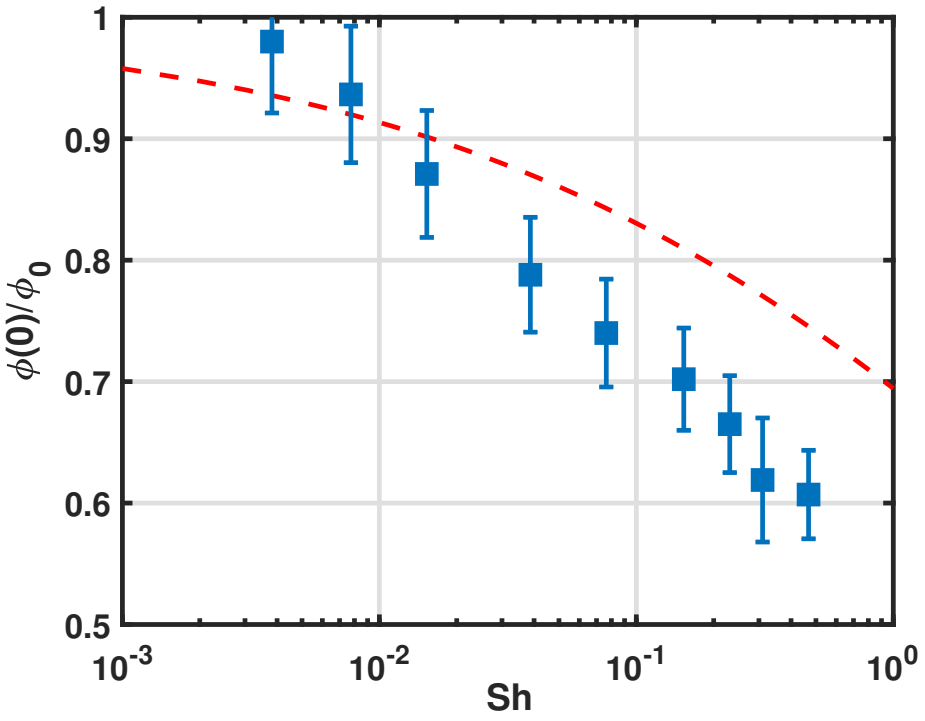

FIG. 18. Variation of the volume fraction at the bottom of the resuspended suspension, $\phi(0)$, normalized by the concentration in the sediment, ϕ_0, as function of Sh in the case of cubic particles (blue squares) and spheres (red dashed line)[14]. The experimental data (blue squares) are determined using eqs. (15) and (20) with the fitting parameters $C = 1.23$, and $n = 1/3$. The error bars are computed based on the uncertainties in the measurements of h_s and h_0 (see Table II).

of resuspension), ϕ_0 (Eq. 15)

Since it is quite difficult to accurately control the mass of particles poured in the Couette gap and then to know the exact total volume of sediment (mainly because of the presence of a meniscus at the suspension-mercury interface), we decided to measure ϕ_0 outside the experimental set-up. By introducing a known mass m_p of cubic particles in a graduated cylinder of well-known section $A_S \sim 1\,cm^2$, filled of the same suspending liquid (*Cargille* oil) and waiting for the particles to fully settle (around $24h$), we measured accurately the sediment height h_{sed} in the tube and deduced: $\phi_0 = m_p/\rho_p \times 1/(h_{sed}A_S) \approx 0.443 \pm 0.001$. Note that this value of ϕ_0 is much smaller than that expected in the case of bead suspensions ($\phi_0 \sim 0.6$).

Figure 18 shows the relative variation of volume fraction at the bottom of the suspension,

$\phi(0)/\phi_0$, as function of the macroscopic Shields number, *Sh*. $\phi(0)$ is deduced from the measurement of h_S and Eq. (15) with $\phi_0 = 0.443$, coupled with Eq. (20) with the following parameters: $C = 1.23$ and $n = 1/3$. As expected, $\phi(0)$ decreases when *Sh* (i.e. $\dot{\gamma}$) increases, ranging from 0.43 ± 0.03 to 0.27 ± 0.02 as *Sh* increases from 3×10^{-3} to 0.5 (corresponding to an increase of $\dot{\gamma}$ from 0.1 to $13\,s^{-1}$). For spherical particles, previous studies[14,47] have shown that $\phi(0)$ varies approximately from 0.57 to 0.45 within the same range of *Sh*. Since $\phi_0|_{cubes} < \phi_0|_{spheres}$, the values of $\phi(0)$ for cubic particles are expected to be consistently lower than those for spherical particles. More interestingly, the relative variation of $\phi(0)$ (i.e. $\phi(0)/\phi_0$) for cubic particles, as shown in Fig. 18, exhibits a much greater variation than that observed for spherical particles, which is consistent with the larger sediment expansion shown in Fig. 17.

3. Normal viscosity

Figure 19 (a) displays the variation of $\lambda_3\eta_n$ deduced from Eq. (14), as function of the concentration at the bottom of the suspension, $\phi(0)$. The data obtained for cubic particles are displayed as blues squares. The solid blue line displays the variation of $\lambda_3\eta_n$ as function of ϕ following Eq. (18) with $K_Z \approx 13$. For the sake of comparison, the results obtained by Acrivos, Mauri, and Fan[45] and Zarraga, Hill, and Leighton Jr[14] for $Sh > 10^{-2}$ are also shown (dashed line) and the dotted line corresponds to an extrapolation (Eq. 18) of their results for smaller *Sh* numbers. Hence, $\lambda_3\eta_n$ is significantly higher for cubic particles than for beads at a given particle volume fraction. The difference observed between suspensions of spheres and suspensions of cubic particles is, of course, less pronounced when $\lambda_3\eta_n$ is plotted as a function of ϕ/ϕ_0. The difference between suspensions of cubes and spheres becomes even smaller when $\lambda_3\eta_n$ is plotted as a function of ϕ/ϕ_m, where ϕ_m is the stress-dependent jamming volume fraction determined from parallel-plate rheometry using the smaller-sized cubes. An important consequence of this is that the ratio $\Sigma^p_{33}/\Sigma_{12}$ appears to be of the same order of magnitude in both spherical and cubic particle suspensions. The inset in Fig. 19 shows the variation of the shear stress across the different resuspension experiments. The shear stress was calculated using the stress-dependent viscosity (see Eq. 12 and Fig. 8), multiplied by the macroscopic shear rate, as defined in Eq.19. As the Shields number decreases (i.e., as ϕ increases), the shear stress initially decreases relatively slowly, then rises sharply at the highest volume fractions (or lowest *Sh* values). This sharp increase in shear stress at high ϕ accounts for the fact that $\lambda_3\eta_n$ could not be plotted as a function of ϕ/ϕ_m for the two highest volume fractions

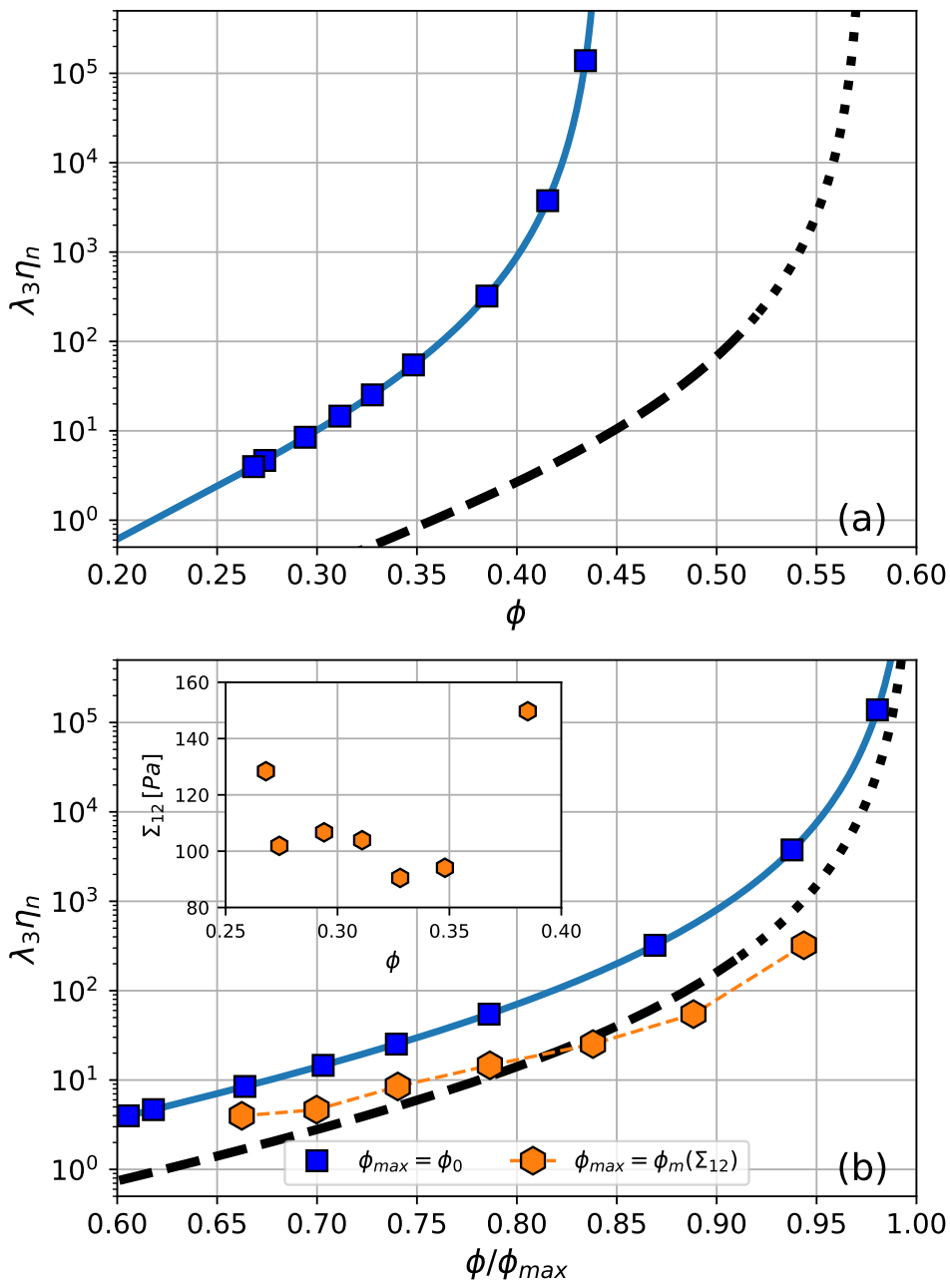

FIG. 19. Variation of $\lambda_3\eta_n$, deduced from Eq. 14, as function of (a) the concentration ϕ and (b) ϕ divided by the packing fraction in the sediment ϕ_0 (squares) and by the stress-dependent jamming volume fraction $\phi_m(\Sigma_{12}$ obtained from viscosity measurements using the smaller-sized cubes (hexagons). The variation reported by Zarraga, Hill, and Leighton Jr [14] for a suspension of spherical particles is also shown: the dashed line corresponds to $Sh > 10^{-2}$, and the dotted line is an extrapolation based on the results of Acrivos, Fan, and Mauri [85] and Zarraga, Hill, and Leighton Jr [14].

($\phi = 0.41$ and 0.433). In these cases, the shear stress exceeded $150\,Pa$, which corresponds to the upper limit at which reliable viscosity measurements could be performed without the onset of edge fracture.

To conclude this section, we recall that the viscous resuspension of cubic particles follows the same type of scaling law as that of spherical particles but occurs in a much more efficient manner, in the sense that, for a given shear stress the sediment expands significantly more than in suspensions of spheres. This similar behavior is particularly consistent with the work of Estrada, Taboada, and Radjai[73], Estrada *et al.*[74], who numerically demonstrated in two dimensions that the mechanical behavior of a dry assembly of regular polygonal particles can be approximated by that of a dry assembly of disks, by accounting for the effect of angular shape through a rolling resistance. This rolling resistance notably enhances the normal forces between particles, which naturally manifests as much higher particle normal stresses in suspensions of cubic particles compared to suspensions of spherical particles. Nonetheless, the ratio of the particle normal stress to shear stress sems to be comparable. Investigating $\mu(J)$ rheology with a device similar to that developed by Etcheverry, Forterre, and Metzger[86] would be highly valuable.

V. CONCLUDING REMARKS

This study represents a step forward in the characterization of the rheology of suspensions of cubic-like particles that is crucial for numerous industrial and geophysical applications.

To conduct this study, we used a microfabrication technique based on soft lithography to produce well-defined cubic particles with characteristic dimensions of several tens of micrometers. This approach allowed us to generate monodisperse cubic suspensions and systematically investigate their rheological properties. Our experiments focused on measuring the shear viscosity as well as the particle normal stresses in order to characterize the full rheological response of these suspensions.

The viscosity measurements revealed several key features. First, in the dilute and semi-dilute regimes, we determined the Einstein and Batchelor coefficients, which characterize the intrinsic viscosity and the role of pairwise hydrodynamic interactions, respectively. The values obtained for cubic particles are larger than those for spherical particles, indicating an enhancement of hydrodynamic interactions due to the angular shape of the cubes. Second, in the dense regime, shear-thinning behavior is clearly observed. While this phenomenon is well-documented for spherical

suspensions, the physical origin of shear-thinning in cubic suspensions remains to be fully understood. Possible explanations include the effect of sliding and rolling friction between particles. Third, the variation of viscosity with volume fraction shows a much lower jamming fraction compared to spheres. This observation is consistent with previous studies on faceted particles in suspensions[21,49] and in granular media[73,74] and suggests that the presence of sharp edges and rolling resistance plays a crucial role in determining the maximum packing fraction.

In addition to viscosity measurements, we performed viscous resuspension experiments to investigate particle normal stresses. Using a methodology based on sediment expansion[14], we demonstrated that suspensions of cubic particles undergo significantly more efficient resuspension than those of spheres. Specifically, for a given shear stress, the sediment expands substantially more in suspensions of cubes than in spherical particle suspensions. This observation indicates that particle normal stresses in cubic suspensions are significantly higher than in their spherical counterparts. The enhanced particle normal stresses are likely a consequence of the shape-induced rolling resistance, which prevents free rotation and leads to an increase in interparticle normal forces.

The main difference between suspensions of cubes and spheres lies in the lower values of ϕ_m observed for cubes, which result in higher viscosities and larger particle normal stresses at a given volume fraction. Aside from this difference, however, the overall rheological behavior shows many similarities between the two systems. In particular, the ratio $\Sigma^p_{33}/\Sigma_{12}$ remains of the same order of magnitude for both suspensions of spheres and cubes. While our results provide a first quantitative characterization of the shear viscosity and particle normal stresses in cubic suspensions, several questions remain open. Future research should aim at developing a theoretical framework to explain the observed shear-thinning behavior and the strong increase in particle normal stresses. Finally, investigating the $\mu(J)$ rheology of these suspensions using the capillary stress-controlled rheometer developed by Etcheverry, Forterre, and Metzger[86] would be of considerable interest.

ACKNOWLEDGEMENTS

We are grateful to Laurent Lobry and François Peters for fruitful discussions and to Sandra Bosio and Christophe Pitiot for technical support. We thank the anonymous reviewers for their constructive comments and suggestions, which helped improve the clarity of the manuscript. In particular, we are grateful for the suggestion to plot Σ^p_{33} as a function of ϕ/ϕ_m, which provided a

more meaningful comparison with existing data on spherical particles.

The authors report no conflict of interest.

REFERENCES

[1]A. Einstein, "Zur theorie der brownschen bewegung," Annalen der physik **324**, 371–381 (1906).

[2]G. Batchelor, "The effect of brownian motion on the bulk stress in a suspension of spherical particles," Journal of fluid mechanics **83**, 97–117 (1977).

[3]S. H. Maron and P. E. Pierce, "Application of ree-eyring generalized flow theory to suspensions of spherical particles," Journal of colloid science **11**, 80–95 (1956).

[4]A. Papadopoulou, J. J. Gillissen, H. J. Wilson, M. K. Tiwari, and S. Balabani, "On the shear thinning of non-brownian suspensions: Friction or adhesion?" Journal of Non-Newtonian Fluid Mechanics **281**, 104298 (2020).

[5]J. A. Richards, B. M. Guy, E. Blanco, M. Hermes, G. Poy, and W. C. Poon, "The role of friction in the yielding of adhesive non-brownian suspensions," Journal of Rheology **64**, 405–412 (2020).

[6]D. Gilbert, R. Valette, and E. Lemaire, "Impact of particle stiffness on shear-thinning of non-brownian suspensions," Journal of Rheology **66**, 161–176 (2022).

[7]R. Mari, R. Seto, J. F. Morris, and M. M. Denn, "Shear thickening, frictionless and frictional rheologies in non-brownian suspensions," Journal of Rheology **58**, 1693–1724 (2014).

[8]R. Seto, R. Mari, J. F. Morris, and M. M. Denn, "Discontinuous shear thickening of frictional hard-sphere suspensions," Physical review letters **111**, 218301 (2013).

[9]S. Gallier, E. Lemaire, F. Peters, and L. Lobry, "Rheology of sheared suspensions of rough frictional particles," Journal of Fluid Mechanics **757**, 514–549 (2014).

[10]H. Barnes, "Shear-thickening ("dilatancy") in suspensions of nonaggregating solid particles dispersed in newtonian liquids," Journal of Rheology **33**, 329–366 (1989).

[11]B. Guy, M. Hermes, and W. C. Poon, "Towards a unified description of the rheology of hard-particle suspensions," Physical review letters **115**, 088304 (2015).

[12]J. Comtet, G. Chatté, A. Niguès, L. Bocquet, A. Siria, and A. Colin, "Pairwise frictional profile between particles determines discontinuous shear thickening transition in non-colloidal suspensions," Nature communications **8**, 1–7 (2017).

[13]F. Gadala-Maria and A. Acrivos, "Shear-induced structure in a concentrated suspension of solid spheres," Journal of Rheology **24**, 799–814 (1980).

[14]I. E. Zarraga, D. A. Hill, and D. T. Leighton Jr, "The characterization of the total stress of concentrated suspensions of noncolloidal spheres in newtonian fluids," Journal of Rheology **44**, 185–220 (2000).

[15]A. Vázquez-Quesada, R. I. Tanner, and M. Ellero, "Shear thinning of noncolloidal suspensions," Physical review letters **117**, 108001 (2016).

[16]A. Vázquez-Quesada, A. Mahmud, S. Dai, M. Ellero, and R. I. Tanner, "Investigating the causes of shear-thinning in non-colloidal suspensions: Experiments and simulations," Journal of Non-Newtonian Fluid Mechanics **248**, 1–7 (2017).

[17]L. Lobry, E. Lemaire, F. Blanc, S. Gallier, and F. Peters, "Shear thinning in non-brownian suspensions explained by variable friction between particles," (2019).

[18]M. Arshad, A. Maali, C. Claudet, L. Lobry, F. Peters, and E. Lemaire, "An experimental study on the role of inter-particle friction in the shear-thinning behavior of non-Brownian suspensions," Soft Matter **17**, 6088–6097 (2021), publisher: The Royal Society of Chemistry.

[19]G. Chatté, J. Comtet, A. Niguès, L. Bocquet, A. Siria, G. Ducouret, F. Lequeux, N. Lenoir, G. Ovarlez, and A. Colin, "Shear thinning in non-brownian suspensions," Soft matter **14**, 879–893 (2018).

[20]G. Ovarlez, F. Mahaut, S. Deboeuf, N. Lenoir, S. Hormozi, and X. Chateau, "Flows of suspensions of particles in yield stress fluids," Journal of rheology **59**, 1449–1486 (2015).

[21]F. Blanc, E. d'Ambrosio, L. Lobry, F. Peters, and E. Lemaire, "Universal scaling law in frictional non-brownian suspensions," Physical Review Fluids **3**, 114303 (2018).

[22]É. Guazzelli and O. Pouliquen, "Rheology of dense granular suspensions," Journal of Fluid Mechanics **852** (2018).

[23]D. J. Pine, J. P. Gollub, J. F. Brady, and A. M. Leshansky, "Chaos and threshold for irreversibility in sheared suspensions," Nature **438**, 997–1000 (2005).

[24]B. Metzger and J. E. Butler, "Irreversibility and chaos: Role of long-range hydrodynamic interactions in sheared suspensions," Physical Review E **82**, 051406 (2010).

[25]B. Metzger, P. Pham, and J. E. Butler, "Irreversibility and chaos: Role of lubrication interactions in sheared suspensions," Physical Review E **87**, 052304 (2013).

[26]M. M. Denn and J. F. Morris, "Rheology of non-brownian suspensions," Annual review of chemical and biomolecular engineering **5**, 203–228 (2014).

[27]R. J. Phillips, R. C. Armstrong, R. A. Brown, A. L. Graham, and J. R. Abbott, "A constitutive equation for concentrated suspensions that accounts for shear-induced particle migration,"

Physics of Fluids A: Fluid Dynamics **4**, 30–40 (1992).

[28]B. Snook, J. E. Butler, and É. Guazzelli, "Dynamics of shear-induced migration of spherical particles in oscillatory pipe flow," Journal of Fluid Mechanics **786**, 128 (2016).

[29]M. Sarabian, M. Firouznia, B. Metzger, and S. Hormozi, "Fully developed and transient concentration profiles of particulate suspensions sheared in a cylindrical couette," arXiv preprint arXiv:1906.03068 (2019).

[30]A. Rashedi, G. Ovarlez, and S. Hormozi, "Engineered transparent emulsion to optically study particulate flows in yield stress fluids," Experiments in Fluids **61**, 1–13 (2020).

[31]A. Badia, Y. D'Angelo, F. Peters, and L. Lobry, "Frame-invariant modeling for non-brownian suspension flows," Journal of Non-Newtonian Fluid Mechanics **309**, 104904 (2022).

[32]M. Orsi, L. Lobry, E. Lemaire, and F. Peters, "Mass and momentum balance during particle migration in the pressure-driven flow of frictional non-brownian suspensions," Journal of Fluid Mechanics **998**, A16 (2024).

[33]F. Boyer, É. Guazzelli, and O. Pouliquen, "Unifying suspension and granular rheology," Physical review letters **107**, 188301 (2011).

[34]A. Singh, R. Mari, M. M. Denn, and J. F. Morris, "A constitutive model for simple shear of dense frictional suspensions," Journal of Rheology **62**, 457–468 (2018).

[35]W. Chèvremont, B. Chareyre, and H. Bodiguel, "Quantitative study of the rheology of frictional suspensions: Influence of friction coefficient in a large range of viscous numbers," Physical Review Fluids **4**, 064302 (2019).

[36]R. V. More and A. M. Ardekani, "Effect of roughness on the rheology of concentrated non-brownian suspensions: A numerical study," Journal of Rheology **64**, 67–80 (2020).

[37]A. V. N. Le, A. Izzet, G. Ovarlez, and A. Colin, "Solvents govern rheology and jamming of polymeric bead suspensions," Journal of Colloid and Interface Science **629**, 438–450 (2023).

[38]R. Hampton, A. Mammoli, A. Graham, N. Tetlow, and S. Altobelli, "Migration of particles undergoing pressure-driven flow in a circular conduit," Journal of Rheology **41**, 621–640 (1997).

[39]A. Graham, S. Altobelli, E. Fukushima, L. Mondy, and T. Stephens, "Note: Nmr imaging of shear-induced diffusion and structure in concentrated suspensions undergoing couette flow," Journal of Rheology **35**, 191–201 (1991).

[40]J. Abbott, N. Tetlow, A. Graham, S. Altobelli, E. Fukushima, L. Mondy, and T. Stephens, "Experimental observations of particle migration in concentrated suspensions: Couette flow," Journal of rheology **35**, 773–795 (1991).

[41]A. W. Chow, S. W. Sinton, J. H. Iwamiya, and T. S. Stephens, "Shear-induced particle migration in couette and parallel-plate viscometers: Nmr imaging and stress measurements," Physics of Fluids **6**, 2561–2576 (1994).

[42]A. W. Chow, J. Iwayima, S. W. Sinton, and D. Leighton, "Particle migration of non-brownian, concentrated suspensions in a truncated cone-and-plate," in *Society of Rheology Meeting, Sacramento, CA*, Vol. 103 (1995) p. 22.

[43]J. F. Morris and F. Boulay, "Curvilinear flows of noncolloidal suspensions: The role of normal stresses," Journal of rheology **43**, 1213–1237 (1999).

[44]P. R. Nott and J. F. Brady, "Pressure-driven flow of suspensions: simulation and theory," Journal of Fluid Mechanics **275**, 157–199 (1994).

[45]A. Acrivos, R. Mauri, and X. Fan, "Shear-induced resuspension in a couette device," International journal of multiphase flow **19**, 797–802 (1993).

[46]B. Saint-Michel, S. Manneville, S. Meeker, G. Ovarlez, and H. Bodiguel, "X-ray radiography of viscous resuspension," Physics of Fluids **31**, 103301 (2019).

[47]E. d'Ambrosio, F. Blanc, and E. Lemaire, "Viscous resuspension of non-brownian particles: determination of the concentration profiles and particle normal stresses," Journal of Fluid Mechanics **911** (2021).

[48]S. Mueller, E. Llewellin, and H. Mader, "The effect of particle shape on suspension viscosity and implications for magmatic flows," Geophysical Research Letters **38** (2011).

[49]H. Hafid, G. Ovarlez, F. Toussaint, P. Jezequel, and N. Roussel, "Effect of particle morphological parameters on sand grains packing properties and rheology of model mortars," Cement and Concrete Research **80**, 44–51 (2016).

[50]R. K. Mallavajula, D. L. Koch, and L. A. Archer, "Intrinsic viscosity of a suspension of cubes," Physical Review E **88**, 052302 (2013).

[51]D. J. Audus, A. M. Hassan, E. J. Garboczi, and J. F. Douglas, "Interplay of particle shape and suspension properties: a study of cube-like particles," Soft matter **11**, 3360–3366 (2015).

[52]C. D. Cwalina, K. J. Harrison, and N. J. Wagner, "Rheology of cubic particles suspended in a newtonian fluid," Soft Matter **12**, 4654–4665 (2016).

[53]M. E. Helgeson, S. C. Chapin, and P. S. Doyle, "Hydrogel microparticles from lithographic processes: Novel materials for fundamental and applied colloid science," Current opinion in colloid & interface science **16**, 106–117 (2011).

[54]A. Sierou and J. F. Brady, "Rheology and microstructure in concentrated noncolloidal suspen-

sions," Journal of Rheology **46**, 1031–1056 (2002).

[55]K. Yeo and M. R. Maxey, "Ordering transition of non-brownian suspensions in confined steady shear flow," Physical Review E **81**, 051502 (2010).

[56]F. Blanc, E. Lemaire, A. Meunier, and F. Peters, "Microstructure in sheared non-brownian concentrated suspensions," Journal of rheology **57**, 273–292 (2013).

[57]N. Wagner and A. M. Woutersen, "The viscosity of bimodal and polydisperse suspensions of hard spheres in the dilute limit," Journal of Fluid Mechanics **278**, 267–287 (1994).

[58]N. Ouchiyama and T. Tanaka, "Porosity of a mass of solid particles having a range of sizes," Industrial & Engineering Chemistry Fundamentals **20**, 66–71 (1981).

[59]S. Pednekar, J. Chun, and J. F. Morris, "Bidisperse and polydisperse suspension rheology at large solid fraction," Journal of Rheology **62**, 513–526 (2018).

[60]A. Poslinski, M. Ryan, R. Gupta, S. Seshadri, and F. Frechette, "Rheological behavior of filled polymeric systems ii. the effect of a bimodal size distribution of particulates," Journal of Rheology **32**, 751–771 (1988).

[61]I. Srivastava, S. A. Roberts, J. T. Clemmer, L. E. Silbert, J. B. Lechman, and G. S. Grest, "Jamming of bidisperse frictional spheres," Physical Review Research **3**, L032042 (2021).

[62]H. A. Scheraga, "Non-newtonian viscosity of solutions of ellipsoidal particles," The Journal of Chemical Physics **23**, 1526–1532 (1955).

[63]D. Merhi, E. Lemaire, G. Bossis, and F. Moukalled, "Particle migration in a concentrated suspension flowing between rotating parallel plates: Investigation of diffusion flux coefficients," Journal of Rheology **49**, 1429–1448 (2005).

[64]M. Keentok and S.-C. Xue, "Edge fracture in cone-plate and parallel plate flows," Rheologica acta **38**, 321–348 (1999).

[65]I. M. Krieger and T. J. Dougherty, "A mechanism for non-newtonian flow in suspensions of rigid spheres," Trans. Soc. Rheol **3**, 137–152 (1959).

[66]E. Lemaire, F. Blanc, C. Claudet, S. Gallier, L. Lobry, and F. Peters, "Rheology of non-brownian suspensions: a rough contact story," Rheologica Acta **62**, 253–268 (2023).

[67]F. Blanc, F. Peters, and E. Lemaire, "Experimental signature of the pair trajectories of rough spheres in the shear-induced microstructure in noncolloidal suspensions," Physical review letters **107**, 208302 (2011).

[68]P. Pham, B. Metzger, and J. E. Butler, "Particle dispersion in sheared suspensions: Crucial role of solid-solid contacts," Physics of Fluids **27** (2015).

[69]E. Brown, N. A. Forman, C. S. Orellana, H. Zhang, B. W. Maynor, D. E. Betts, J. M. DeSimone, and H. M. Jaeger, "Generality of shear thickening in dense suspensions," Nature materials **9**, 220–224 (2010).

[70]C. Wildemuth and M. Williams, "Viscosity of suspensions modeled with a shear-dependent maximum packing fraction," Rheologica acta **23**, 627–635 (1984).

[71]J. Z. Zhou, P. H. Uhlherr, and F. T. Luo, "Yield stress and maximum packing fraction of concentrated suspensions," Rheologica acta **34**, 544–561 (1995).

[72]J. F. Morris, "Progress and challenges in suspension rheology," Rheologica Acta **62**, 617–629 (2023).

[73]N. Estrada, A. Taboada, and F. Radjai, "Shear strength and force transmission in granular media with rolling resistance," Physical Review E **78**, 021301 (2008).

[74]N. Estrada, E. Azéma, F. Radjai, and A. Taboada, "Identification of rolling resistance as a shape parameter in sheared granular media," Physical Review E **84**, 011306 (2011).

[75]A. Singh, C. Ness, R. Seto, J. J. de Pablo, and H. M. Jaeger, "Shear thickening and jamming of dense suspensions: the "roll" of friction," Physical Review Letters **124**, 248005 (2020).

[76]E. d'Ambrosio, D. L. Koch, and S. Hormozi, "The role of rolling resistance in the rheology of wizarding quidditch ball suspensions," Journal of Fluid Mechanics **974**, A36 (2023).

[77]A. Singh, G. L. Jackson, M. van der Naald, J. J. de Pablo, and H. M. Jaeger, "Stress-activated constraints in dense suspension rheology," Physical Review Fluids **7**, 054302 (2022).

[78]M. A. Benmebarek and M. Movahedi Rad, "Effect of rolling resistance model parameters on 3d dem modeling of coarse sand direct shear test," Materials **16**, 2077 (2023).

[79]F. Peters, G. Ghigliotti, S. Gallier, F. Blanc, E. Lemaire, and L. Lobry, "Rheology of non-brownian suspensions of rough frictional particles under shear reversal: A numerical study," Journal of rheology **60**, 715–732 (2016).

[80]N. Y. Lin, B. M. Guy, M. Hermes, C. Ness, J. Sun, W. C. Poon, and I. Cohen, "Hydrodynamic and contact contributions to continuous shear thickening in colloidal suspensions," Physical review letters **115**, 228304 (2015).

[81]E. d'Ambrosio, F. Blanc, and E. Lemaire, "The characterization of the particle normal stresses of concentrated granular suspensions by local rheometry," Journal of Fluid Mechanics **967**, A34 (2023).

[82]D. Leighton and A. Acrivos, "The shear-induced migration of particles in concentrated suspensions," Journal of Fluid Mechanics **181**, 415–439 (1987).

[83]A. Badia, E. d'Ambrosio, Y. d'Angelo, F. Peters, and L. Lobry, "Three-dimensional numerical investigation of a suspension flow in an eccentric couette flow geometry," Physics of Fluids **36** (2024).

[84]G. Ovarlez, F. Bertrand, and S. Rodts, "Local determination of the constitutive law of a dense suspension of noncolloidal particles through magnetic resonance imaging," Journal of rheology **50**, 259–292 (2006).

[85]A. Acrivos, X. Fan, and R. Mauri, "On the measurement of the relative viscosity of suspensions," Journal of Rheology **38**, 1285–1296 (1994).

[86]B. Etcheverry, Y. Forterre, and B. Metzger, "Capillary-stress controlled rheometer reveals the dual rheology of shear-thickening suspensions," Physical Review X **13**, 011024 (2023).